INRIA

INSTITUT NATIONAL DE RECHERCHE EN INFORMATIQUE ET EN AUTOMATIQUE

Pressure image assimilation for atmospheric motion estimation

Thomas Corpetti — Patrick Héas — Etienne Mémin — Nicolas Papadakis

N° 6507

Avril 2008

Thème COG

ISSN 0249-6399 ISRN INRIA/RR--6507--FR+ENG

Pressure image assimilation for atmospheric motion estimation

Thomas Corpetti* †, Patrick Héas‡, Etienne Mémin*§¶, Nicolas Papadakis‖

Thème COG — Systèmes cognitifs
Équipes-Projets Vista

Rapport de recherche n° 6507 — Avril 2008 — 37 pages

Abstract: The complexity of dynamical laws governing 3D atmospheric flows associated with incomplete and noisy observations makes the recovery of atmospheric dynamics from satellite images sequences very difficult. In this report, we face the challenging problem of estimating physical sound and time-consistent horizontal motion fields at various atmospheric depths for a whole image sequence. Based on a vertical decomposition of the atmosphere, we propose two dynamically consistent atmospheric motion estimators relying on different multi-layer dynamical models. Both estimators use a framework derived from data assimilation and are applied on noisy and incomplete pressure difference observations derived from satellite images. In the first model, dense pressure difference maps are reconstructed according to a shallow-water model on each cloud layer. While performing this reconstruction, the variational process estimates the average horizontal wind fields of the multi-layer model. The second model relies on a simplified vorticity-divergence form of the previous multi-layer shallow-water model. In this case, average horizontal motion fields are estimated for each layer without reconstructing pressure maps. While the simplified model is not as precise as the exact shallow-water model, the latter estimator exploits finer spatio-temporal image structures and succeeds in characterizing motion at smaller spatial scales. The performance of both methods is assessed on synthetic examples and on real world meteorological satellite image sequences.

Key-words: Variational assimilation, motion estimation, atmospheric motions, pressure images, shallow-water models, atmospheric dynamics

* IRISA - Campus de Beaulieu - 35042 Rennes cedex -France.
† CNRS / COSTEL UMR 6554, Place du Recteur Henri Le Moal, 35043 Rennes Cedex, France
‡ CEMAGREF - Avenue de Cucillé- 35044 Rennes cedex -France
§ CEFIMAS, Avenida Santa Fe 1145 C1059ABF - Buenos Aires, Argentina
¶ Fac. de Ing. de la Univ. Buenos-Aires, Av. Paseo Colón 850, C1063ACV Buenos Aires, Argentina
‖ UPF/Passeig de Circumvallació, 8 08003 Barcelona

Centre de recherche INRIA Rennes – Bretagne Atlantique
IRISA, Campus universitaire de Beaulieu, 35042 Rennes Cedex
Téléphone : +33 2 99 84 71 00 —Télécopie : +33 2 99 84 71 71

Assimilation d'images de pression pour l'estimation de mouvements atmosphériques

Résumé : La complexité des lois dynamiques régissant les flux atmosphériques 3D, associée à des observations bruitées et incomplètes issues d'images satellitales, rend difficile l'estimation de paramètres liés à la dynamique de l'atmosphère. Dans ce rapport, nous nous concentrons sur le difficile problème d'estimation consistante dans le temps de mouvements horizontaux à différentes altitudes de l'atmosphère à partir d'une séquence d'images. Sur la base d'une décomposition verticale de l'atmosphère, nous proposons deux estimateurs de mouvements consistants temporellement et s'appuyant sur différents modèles dynamiques multicouches. Les deux estimateurs utilisent un cadre théorique dérivé de l'assimilation de données et sont appliqués à des observations bruitées et incomplètes d'images de différence de pression obtenues à partir de données satellitaires. Dans le premier modèle, des cartes denses de différence de pression sont reconstruites selon un modèle shallow-water exact sur chaque couche nuageuse. En sus de cette reconstruction, le processus variationnel estime les champs de vents horizontaux moyens liés au modèle multi-couche utilisé. Le second modèle repose sur un modèle simplifié du précédent et est formulé en termes de vorticité-divergence. Dans ce cas, les champs moyens horizontaux sont estimés dans chaque couche sans reconstruction des cartes de pression. Bien que le modèle simplifié ne soit pas aussi précis que le modèle exact shallow-water, il extrait des structures spatio-temporelles plus fines et est en mesure de caractériser le mouvement à petites échelles spatiales. La performance et la comparaison des deux méthodes est évaluée sur des exemples synthétiques et réels issus d'images satellites météorologiques.

Mots-clés : Assimilation variationnelle, estimation du mouvement, mouvements atmosphériques, Images de pression, Modèles shallow-water, Dynamique atmosphérique

1 Introduction

1.1 Overview

Geophysical motion characterization and image sequence analysis are crucial issues for numerous scientific domains involved in the study of climate change, weather forecasting, climate prediction or biosphere analysis. The use of surface station, balloon or in-flight aircraft measurements has improved the estimation of wind fields and has been a subsequent step for a better understanding of meteorological phenomena. However, the network's temporal and spatial resolutions may be insufficient for the analysis of mesoscale dynamics. Recently, in an effort to avoid these limitations, high resolution satellites sensors have been designed to provide image sequences characterized by finer spatial and temporal resolutions. Nevertheless, the analysis of atmospheric motion from image sequences remains particularly challenging due to the complexity of atmospheric dynamics observed at such scales. Thus advanced techniques are needed to exploit the new generation of satellite images.

1.2 Related works

In the context of image-based geophysical motion analysis, standard techniques from computer vision, originally designed for bi-dimensional quasi-rigid motions with stable salient features, appear to be not well adapted [22, 18]. The design of techniques dedicated to fluid flows has been a step forward, towards the constitution of reliable methods to extract characteristic features of flows [42, 4, 3, 6, 41]. However, for geophysical applications, existing fluid-dedicated methods are all limited to frame to frame estimation and do not rely on physical conservation laws.

Geophysical flows are quite well described by appropriate physical models. As a consequence in such contexts, the inclusion of the law of physical evolution should be a very powerful means for the motion analyzes of satellite image data, in comparison to standard variational or statistical generic image based motion estimation techniques.

Recently, a layered motion estimator based on the shallow water mass conservation equation has been proposed in [14, 13]. In these works, time consistency is reinforced by the introduction of a frame to frame temporal regularization based on a simplified vorticity-divergence form of the shallow water momentum conservation equations.

Variational data assimilation [21, 36], derived from optimal control theory [23], offers an efficient framework to deal with physical models and different kind of observations. Since its introduction, the variational assimilation technique commonly known as 4D-Var has been widely used for global atmospheric numerical weather forcasting or climate numerical modeling [1, 2, 12, 35]. Different variations of the original principles have been proposed since the last 15 years [1, 5, 20] and this technique is routinely used in several operational meteorological center.

Although image observations possess very good spatial resolutions compared to spatial scales of standard data, only very few attempts have been done to date

to consider their use. As a matter of fact, the projection on the image plane of the three dimensional observed quantity and the complexity of the phenomenon involved in the image formation make this issue considerably difficult.

Variational data assimilation techniques relying on image data or on features extracted from image data have been recently proposed. A technique for the assimilation of a low order dynamical system, obtain from a POD-Galerkin projection, has been proposed in [7]. This technique makes use of noisy flow motion measurements estimated from a set of pairs of images of particles. In [31], an optimal control strategy has been proposed for the recovery of fluid motion. This approach based on a Stokes flow model remains nevertheless an estimation technique that works only on two consecutive frames and no dynamical coherency can be guaranteed. In a different spirit, two different variational assimilation strategies have been proposed in the computer vision community for the tracking of curves [30] and the estimation of fluid motion fields [28]. Both of these methods directly assimilate image data. They do not depend on pseudo-measurements extracted by external techniques but rather propose to include directly a differential observation operator issued from image features estimation methods.

The two techniques proposed in this paper constitute extensions of these previous approaches to atmospheric motion estimation from satellite image sequences.

1.3 Contributions

The two methods proposed in this paper differ significantly from previous works on motion analysis by satellite imagery. Indeed, as opposed to previous image-based techniques relying on two consecutive frames, the proposed methods estimate dynamically consistent motion fields through a whole image sequence.

For the first method, this is done through a variational approach derived from the data assimilation principle. It combines a large scale multi-layer shallow water dynamical model with filtered pressure difference observations obtained from satellite images. This first method directly extends the standard variational data assimilation recipes to pressure images. In the second proposed method, the assimilation scheme exploits a simplified version of the previous dynamical model which includes uncertainty terms. In contrast to the first approach, this second method incorporates fine scale spatio-temporal image features as observations. This technique is in spirit different from the first approach and from standard data assimilation techniques.

The document is organized as follows. After a description of data assimilation methodology in section 2, the acquisition of pressure image observations is presented in section 3. The two different image assimilation schemes are then successively described in sections 4 and 5. A comparison of the two methods on synthetic and real meteorological images is provided in section 6.

2 Data assimilation

In this section let us recall the variational data assimilation concepts [21, 36, 1] proposed for the analysis of geophysical flows. We will first present a standard formulation where the state variable of interest obeys a perfect evolution law.

Let us note that this situation corresponds to the most usual model used in the geophysical domain for data assimilation.

2.1 Data Assimilation with perfect model

2.1.1 Direct evolution model

Let the state space $\mathcal{V}$ be an Hilbert space identified to its dual space. Noting $X \in \mathcal{W}(t_0, t_f)$ as the state variable representing the feature of interest, which is assumed to live in a functional space $\mathcal{W}(t_0, t_f) = \{X | X \in L^2(t_0, t_f; \mathcal{V}), \partial_t X \in L^2(t_0, t_f; \mathcal{V})\}$ and assuming that the evolution in time range $[t_0; t_f]$ of the state is described through a (non linear) differential model $\mathbb{M} : \mathcal{V} \times]t_0, t_f[\rightarrow \mathcal{V}$, we get the following direct problem:

$$\left|\left| \begin{array}{l} \text{For a given } \eta \in \mathcal{V}, \text{ find } X \in \mathcal{W}(t_0, t_f) \text{ such that:} \\ \left\{ \begin{array}{l} \partial_t X(t) + \mathbb{M}(X(t), t) = 0, \\ X(t_0) = X_0 + \eta. \end{array} \right. \end{array} \right. \tag{1}$$

This system is monitored by a control variable, $\eta \in \mathcal{V}$, identified here as the inaccuracy on the initial condition. The control could also be defined by model parameters [21] or by boundary conditions [38, 40]. The direct problem (1) will be assumed to be well posed, which means that we first assume that the application $\mathcal{V} \rightarrow \mathcal{V} : \eta \mapsto X(\eta, t)$ is differentiable $\forall t \in]t_0, t_f[$ and secondly that given $\eta \in \mathcal{V}$, $\forall t_f > t_0$, there exists a unique function $X \in \mathcal{W}(t_0, t_f)$ as solution of problem (1) and that this solution depends continuously on η, i.e.: $\mathcal{V} \rightarrow \mathcal{V} : \eta \mapsto X(\eta, t)$ is continuous $\forall t \in]t_0, t_f[$. Let us also assume that some observations $Y \in \mathcal{O}$ of the state variable components are available. These observations may live in a different space (a reduced space for instance) from the state variable. We will nevertheless assume that there exists a (non linear) observation operator $\mathbb{H} : \mathcal{V} \rightarrow \mathcal{O}$, that goes from the variable space to the observation space.

2.1.2 Cost function

An error cost function $J : \mathcal{V} \times \mathcal{V} \rightarrow \mathbb{R}$ measuring the discrepancy between a solution associated with a given control and the observations available can be introduced:

$$J(\eta) = \frac{1}{2} \int_{t_0}^{t_f} \|Y - \mathbb{H}(X(\eta, t), t)\|_R^2 dt + \frac{1}{2} \|\eta\|_B^2 . \tag{2}$$

Thus, the overall problem that we are facing consists in finding the control variable $\eta \in \mathcal{V}$ that minimizes cost function J. Norms $\|\cdot\|_R$ and $\|\cdot\|_B$ are respectively associated with the scalar products $\left\langle R^{-1}\cdot, \cdot \right\rangle_{\mathcal{O}}$ and $\left\langle B^{-1}\cdot, \cdot \right\rangle_{\mathcal{V}}$, where R and B are symmetric positive defined endomorphisms of $\mathcal{V}$. In our applications, R and B are respectively called the observation covariance matrix and the initialization covariance matrix.

Algorithm 2.1 *Perfect Model*
Let $X(t_0) = X_0$.

(i) *From* $X(t_0)$*, compute* $X(t)$*,* $\forall t \in]t_0, t_f[$ *with a forward integration of system (1).*

(ii) *With* $X(t)$*, realize a backward integration of the adjoint variable with the system (3).*

(iii) *Update the initial condition* $X(t_0)$ *with relation (5).*

(iv) *Return to* (i) *and repeat until a convergence criterion.*

2.1.3 Adjoint evolution model

The gradient of this functional is computed introducing an adjoint variable λ defined as the solution of the following adjoint problem:

$$\left|\left| \begin{array}{l} \text{Given } \eta \in \mathcal{V},\ t_f > t_0 \text{ and } X(t) \text{ solution of (1)}, \\ \text{find } \lambda \in \mathcal{W}(t_0, t_f) \text{ such that, } \forall t \in]t_0, t_f[: \\ \left\{ \begin{array}{l} -\partial_t \lambda(t) + (\partial_X \mathbb{M})^* \lambda(t) = (\partial_X \mathbb{H})^* R^{-1}(Y - \mathbb{H}(X(t))), \\ \lambda(t_f) = 0. \end{array} \right. \end{array} \right. \tag{3}$$

In the same way as for the direct model, it is assumed that given $\eta \in \mathcal{V}$, $t_f > t_0$ and $X \in \mathcal{W}(t_0, t_f)$ as solution of problem (1), there exists a unique function $\lambda \in \mathcal{W}(t_0, t_f)$ as solution of problem (3). It is also assumed that this solution depends continuously on η (i.e: $\mathcal{V} \to \mathcal{V} : \eta \mapsto \lambda(\eta, t)$ is continuous $\forall t \in]t_0, t_f[$).

2.1.4 Functional gradient

Given this adjoint problem, it can be shown that the cost function derivative with respect to η finally reads:

$$\frac{\partial J}{\partial \eta} = -\lambda(t_0) + B^{-1}(X(t_0) - X_0). \tag{4}$$

As a consequence, given a solution $X(t)$ of the direct model (1), the functional gradient can be computed from a backward integration of the adjoint model (3). The adjoint variable then permits to update the initial condition, by canceling the gradient defined in (4):

$$X(t_0) = X_0 + B\lambda(t_0) \tag{5}$$

where B is the pseudo inverse of B^{-1} [1]. As the complexity of the adjoint model resolution is the same as the one of the direct model, the use of this technique appears to be very efficient for state space of large dimension. The principle of the overall technique is summarized in Algorithm (2.1). This first approach has been widely used in environmental sciences for the analysis of geophysical flows [1, 8, 12, 35]. However, such modeling appears to be limited in image analysis since the differents models, on which we can rely, are usually inaccurate due, for instance, to 3D-2D projections, varying lighting conditions, completely unknown boundary conditions, *etc.* Considering imperfect dynamical models now comes to an optimization problem where the control variable is constituted by the whole trajectory of the state variable.

2.2 Data Assimilation with imperfect model

The dynamical model we consider now is defined up to a control function $\nu \in \mathcal{W}(t_0, t_f, V)$, where $\nu(t) \in \mathcal{V}$. We are now facing an imperfect dynamical system which depends on the whole trajectory of the control variables (i.e ν, η). Formally, the system reads:

$$\left|\left| \begin{array}{l} \text{Given } (\nu, \eta) \in (\mathcal{W}, \mathcal{V}), \text{ find } X \in \mathcal{W}(t_0, t_f) \text{ such that} \\ \left\{ \begin{array}{ll} \partial_t X(t) + \mathbb{M}(X(t), t) = \nu(t) & \forall t \in]t_0, t_f[, \\ X(t_0) = X_0 + \eta. \end{array} \right. \end{array} \right. \tag{6}$$

2.2.1 Cost function

The cost function $J : \mathcal{W} \times \mathcal{V} \to \mathbb{R}$ that gathers the different types of involved errors is defined as:

$$\begin{aligned} J(\nu, \eta) = & \frac{1}{2} \int_{t_0}^{t_f} \|Y - \mathbb{H}(X(\nu(t), \eta, t))\|_R^2 \, dt + \frac{1}{2} \|\eta\|_B^2 \\ & + \frac{1}{2} \int_{t_0}^{t_f} \|\nu(t)\|_Q^2 \, dt. \end{aligned} \tag{7}$$

The norm $\|\cdot\|_Q$ is associated to the inner scalar product $\left\langle Q^{-1} \cdot, \cdot \right\rangle_V$, where Q is a symmetric positive defined endomorphism of $\mathcal{V}$ called the model covariance matrix.

2.2.2 Adjoint evolution model

Similarly to the previous case, defining the adjoint variable $\lambda \in \mathcal{W}(t_0, t_f)$ as a solution of the following adjoint problem:

$$\left|\left| \begin{array}{l} \text{Given } (\nu, \eta) \in (\mathcal{W}, \mathcal{V}),\ t_f > t_0 \text{ and } X(t) \text{ a solution of (6)}, \\ \text{find } \lambda \in \mathcal{W}(t_0, t_f), \text{ such that, } \forall t \in]t_0, t_f[: \\ \left\{ \begin{array}{l} -\partial_t \lambda(t) + (\partial_X \mathbb{M})^* \lambda(t) = (\partial_X \mathbb{H})^* R^{-1} (Y - \mathbb{H}(X(t))), \\ \lambda(t_f) = 0. \end{array} \right. \end{array} \right. \tag{8}$$

enables one to get an expression of the cost function gradient.

2.2.3 Functional gradient

It can be shown that the derivatives of the cost function with respect to ν and η reads in this case:

$$\frac{\partial J}{\partial \nu} = Q^{-1}(\partial_t X + \mathbb{M}(X)) - \lambda, \tag{9}$$

$$\frac{\partial J}{\partial \eta} = -\lambda(t_0) + B^{-1}(X(t_0) - X_0). \tag{10}$$

Canceling these components to zero and introducing Q and B, the respective pseudo inverses of Q^{-1} and B^{-1}, we have:

$$\left\{ \begin{array}{l} \partial_t X(t) + \mathbb{M}(X(t)) = Q\lambda(t) \\ X(t_0) - X_0 = B\lambda(t_0). \end{array} \right. \tag{11}$$

The second equation still constitutes an incremental update of the initial condition. Generalizing these expressions, we can define the following incremental formulation.

Algorithm 2.2 *Imperfect model*
Let $X(t_0) = X_0$.

(i) *From* $X(t_0)$*, compute* $X(t)$*,* $\forall t \in]t_0, t_f[$ *with a forward integration of system (13).*

(ii) $X(t)$ *being given, realize a backward integration of the adjoint variable with the system (8).*

(iii) *Compute the initial value of the incremental function(15).*

(iv) *From* $dX(t_0)$*, compute* $dX(t)$*,* $\forall t \in]t_0, t_f[$ *with a forward integration of system (14).*

(v) *Update* $X = X + dX$.

(vi) *Return to* (ii) *and repeat until convergence.*

2.2.4 Incremental function

Denoting

$$\begin{cases} X(t) = \tilde{X}(t) + dX(t) & \forall t \in [t_0, t_f], \\ \tilde{X}(t_0) = X_0, \end{cases} \tag{12}$$

where $\tilde{X(t)}$ could either be a fixed component or a previous estimated trajectory of the state variable. Equation (11) can be split and written as:

$$\partial_t \tilde{X}(t) + \mathbb{M}(\tilde{X}(t)) = 0 \qquad \forall t \in]t_0, t_f[, \tag{13}$$

$$\partial_t dX(t) + \partial_{\tilde{X}} \mathbb{M}(\tilde{X}(t)) dX(t) = Q\lambda(t) \qquad \forall t \in]t_0, t_f[. \tag{14}$$

Hence, the update of the state variable X is driven by an incremental function dX which depends on the whole trajectory of the adjoint variable λ. The initial value of this incremental function is given by (10):

$$dX(t_0) = B\lambda(t_0). \tag{15}$$

Equations (6), (12), (13), (14) and (15) give rise to the data assimilation method with imperfect dynamical model. A sketch of the whole process is summarized in Algorithm (2.2).

3 Image observations

3.1 Layer decomposition

The layering of atmospheric flow in the troposphere is valid in the limit of horizontal scales much greater than the vertical scale height. Thus for layers of a thickness on the order of scale of 1km, this hypothesis is roughly valid for horizontal scales greater or equal to 100 km. It is thus impossible to truly characterize a layered atmosphere with a local analysis performed in the vicinity of a pixel characterizing a kilometer order scale. Nevertheless, one can still decompose the 3D space into elements of variable thickness, where only sufficiently

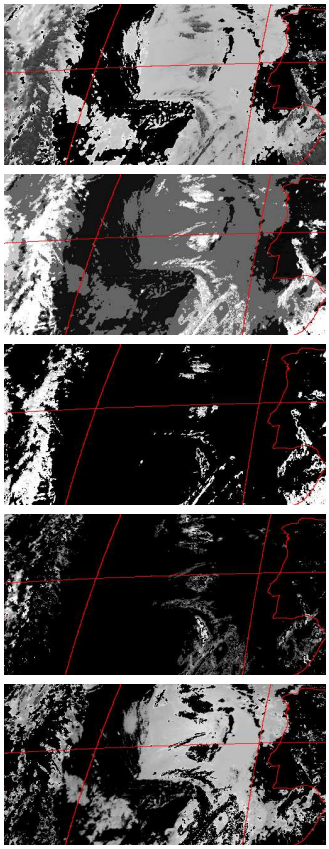

Figure 1: ***Image observations***. *From top to bottom : cloud top pressure image; classification into low (in dark gray), medium (in light gray) and high (in white) clouds; pressure difference of the higher layer; pressure difference of the intermediate layer; pressure difference of the lower layer. Black regions correspond to missing observations and red lines represent coastal contours, meridians and parallels (every* 10^o*).*

thin regions of such elements may really correspond to common layers. Analysis based on such a decomposition presents the main advantage of operating at different atmospheric pressure ranges and avoids the mix of heterogeneous observations.

For the definition of the K layers, we present the 3D space decomposition introduced in [14, 13]. The k-th layer corresponds to the volume lying in between an upper surface s^{k+1} and a lower surface s^k. These surfaces s^{k+1} are defined by the height of top of clouds belonging to the k-th layer. They are thus defined only in areas where there exist clouds belonging to the k-th layer, and remain undefined elsewhere. The membership of top of clouds to the different layers is determined by cloud classification maps, as illustrated in figure 1. Such classifications, which are based on thresholds of top of cloud pressure, are routinely provided by the EUMETSAT consortium, the European agency which supplies the METEOSAT satellite data.

3.2 Sparse pressure difference image observations

Top of cloud pressure images, as routinely provided by the EUMETSAT consortium, are derived from a radiative transfer model using ancillary data obtained by analysis or short term forecasts. Multi-channel techniques enable the determination of the pressure at the top of semi-transparent clouds [33].

We denote by C^k the class corresponding to the k-th layer. Note that the top of cloud pressure image is composed of segments of top of cloud pressure functions $p(s^k)$ related to the different layers. That is to say, cloud pressure image is defined as $\{\bigcup_k p(x,y,s^{k+1},\mathbf{s})|(x,y) \in C^k\}$. Thus, pressure images of top of clouds are used to constitute sparse pressure maps of the layer upper boundaries $p(s^{k+1})$. As with satellite images, the lower cloud boundaries are always occluded, we coarsely approximate the missing pressure observations $p(s^k)$ by an average pressure value $\overline{p}(s^k)$ observed as the top of the clouds of the layer underneath. Finally, for layer $k \in [1,K]$, we define observations h^k_{obs} as pressure differences in hecto Pascal (hPa) units:

$$h^k_{obs} = \begin{cases} \overline{p}(x,y,s^k) - p(x,y,s^{k+1}) & if \quad (x,y) \in C^k \\ 0 & else \end{cases} \tag{16}$$

Resulting image observations are illustrated in figure 1.

4 Image assimilation with a perfect dynamical model

In this section, we will adopt a perfect modeling scheme for atmospheric layers using filtered shallow water equations, while in section 5, we will relax the constraint on the dynamical model accuracy (i.e. on the shallow water assumption) by using an imperfect modeling scheme combined with an appropriate observation operator.

4.1 Shallow-water model for atmospheric layers

In order to provide a dynamical model describing the evolution of pressure difference observations, we use the shallow-water approximation (horizontal motion much greater than vertical motion under the assumption of incompressibility) [9]. This approximation is valid for the upper range of mesoscale analysis in a layered atmosphere. Considering horizontal scales on the order of 100 km, combined with layer depths on the order of 1 km, makes the shallow-water approximation relevant. Therefore, in order to obtain a valid dynamical model on a pixel grid of resolution δ_p in kilometers, we can filter the dynamical equations with a Gaussian kernel function K_{δ_x} of standard deviation equal to $\delta_x = 100\delta_p^{-1}$, where δ_p denotes the image pixel resolution in kilometers.

Shallow-water approximation assumes incompressibility. Thus we consider a constant density $\overline{\rho}^k$ within the layer, which implies under hydrostatic balance that horizontal divergence is weak. Let us remark that this incompressibility simplification which underlies a shallow water system is reasonable, while it may be erroneous for finer horizontal scales. Mean densities $\overline{\rho}^k$ can be related to the average pressures $\overline{p}^k$ by vertical integration of the equation of state for dry air

($p = \rho RT$), combined with the hydrostatic relation ($dp = -g\rho dz$), under the assumption of constant lapse rate ($T = T_0 + \gamma z$), where g, R, T_0 and γ denote the standard physical constants. More precisely, between altitudes z_0 and z (or pressure p_0 and p), one obtains :

$$\int_{p_0}^{p} \frac{dp'}{p'} = -\int_{z_0}^{z} \frac{g}{R(T_0 + \gamma z')} dz', \tag{17}$$

which yields after some calculation to the expression of density as a function of pressure [16]:

$$\rho(p) = \frac{p_0}{RT_0} \left(\frac{p}{p_0}\right)^{\frac{\gamma R}{g}+1}. \tag{18}$$

Thus, computing the vertical average, the mean density related to the k-th layer reads :

$$\begin{aligned} \overline{p}^k &= \frac{1}{\overline{p}^{k+1} - \overline{p}^k} \int_{\overline{p}^k}^{\overline{p}^{k+1}} \rho(p) dp \\ &= \frac{p_0^2}{(\overline{p}^{k+1} - \overline{p}^k)(\frac{\gamma R}{g} + 2) RT_0} \left[\left(\frac{p}{p_0}\right)^{\frac{\gamma R}{g}+2} \right]_{\overline{p}^k}^{\overline{p}^{k+1}}. \end{aligned} \tag{19}$$

Note that a constant lapse rate γ, that is to say a linear variation of temperature with altitude, is a rough approximation in the troposphere. However, as we are averaging the obtained density law vertically and horizontally over the whole domain embedding the layer, the impact of such an assumption should have minor impact on the modeling.

We now derive a direct shallow-water model dedicated to atmospheric layers. At the upper range of the mesoscale, friction components and terms depending on Earth curvature can be neglected [16, 14, 13]. Introducing the filtered pressure and horizontal wind

$$\tilde{p} = K_{\delta_x} * p \tag{20}$$

$$\tilde{\mathbf{v}} = (\tilde{u}, \tilde{v})^T = K_{\delta_x} * (u, v)^T \tag{21}$$

and using the shallow-water approximation, the filtered horizontal momentum equations for atmospheric motion read :

$$\left\{ \begin{array}{rcl} \frac{d\tilde{u}}{dt} + \frac{\tilde{p}_x}{\rho_0} - \tilde{v} f^\phi &=& \nu_{\mathcal{T}} \Delta \tilde{u} \\ \frac{d\tilde{v}}{dt} + \frac{\tilde{p}_y}{\rho_0} + \tilde{u} f^\phi &=& \nu_{\mathcal{T}} \Delta \tilde{v} \end{array} \right. \tag{22}$$

where ρ_0, f^ϕ and $\nu_{\mathcal{T}}$ denote the local mean density, the Coriolis factor depending on latitude ϕ and the turbulent viscosity produced at sub-grid scales [10]. The induced turbulent dissipation can be approached by sub-grid models proposed in large eddy simulation literature [32]. The simplest one is the well known Smagorinsky sub-grid model which is in agreement with Kolmogorov "K41" theory [34]. For 2D flows, it results in an anisotropic diffusion with a turbulent viscosity coefficient equal to :

$$\nu_{\mathcal{T}} = (C\delta_x)^2 \sqrt{2(\tilde{u}_x^2 + \tilde{v}_y^2 + (\tilde{u}_y + \tilde{v}_x)^2)} \tag{23}$$

where C is the Smagorinsky coefficient (which is usually fixed to 0.17).

Expanding the total derivatives in the isobaric coordinate system (x, y, p) and using the fact that the flow is incompressible (zero local 3D divergence), Equation 22 can be rewritten as :

$$\left\{ \begin{array}{rcl} \frac{\partial \tilde{u}}{\partial t} + \frac{\partial \tilde{u}^2}{\partial x} + \frac{\partial \tilde{u}\tilde{v}}{\partial y} + \frac{\partial \tilde{u}\tilde{\omega}}{\partial p} + \frac{\tilde{p}_x}{\rho_0} - \tilde{v} f^\phi & = & \nu_{\mathcal{T}} \Delta \tilde{u} \\ \frac{\partial \tilde{v}}{\partial t} + \frac{\partial \tilde{u}\tilde{v}}{\partial x} + \frac{\partial \tilde{v}^2}{\partial y} + \frac{\partial \tilde{v}\tilde{\omega}}{\partial p} + \frac{\tilde{p}_y}{\rho_0} + \tilde{u} f^\phi & = & \nu_{\mathcal{T}} \Delta \tilde{v} \end{array} \right. \tag{24}$$

where $\tilde{\omega} = \frac{d\tilde{p}}{dt}$ is the filtered vertical wind component in pressure coordinates. In the isobaric coordinate system (x, y, p), the mass conservation equation reads :

$$\frac{\partial \tilde{u}}{\partial x} + \frac{\partial \tilde{v}}{\partial y} + \frac{\partial \tilde{w}}{\partial p} = 0 \tag{25}$$

In order to perform the vertical integration of Equation 24 and Equation 25 in the pressure interval $[\tilde{p}(s^{k+1}), \tilde{p}(s^k)]$, we first fix the boundary conditions :

$$\left\{ \begin{array}{rcl} \frac{\partial \tilde{p}(s^k)}{\partial t} + \tilde{u}(s^k) \frac{\partial \tilde{p}(s^k)}{\partial x} + \tilde{v}(s^k) \frac{\partial \tilde{p}(s^k)}{\partial y} & = & \tilde{\omega}(s^k) \\ \frac{\partial \tilde{p}(s^{k+1})}{\partial t} + \tilde{u}(s^{k+1}) \frac{\partial \tilde{p}(s^{k+1})}{\partial x} + \tilde{v}(s^{k+1}) \frac{\partial \tilde{p}(s^{k+1})}{\partial y} & = & \tilde{\omega}(s^{k+1}). \end{array} \right. \tag{26}$$

Such boundary conditions can be interpreted as the fact that boundary surfaces $\tilde{p}(s^k)$ and $\tilde{p}(s^{k+1})$ are deformed by the vertical wind $\tilde{\omega}(s^k)$ and $\tilde{\omega}(s^{k+1})$. To achieve such a vertical integration in the pressure interval $[\tilde{p}(s^{k+1}), \tilde{p}(s^k)]$ varying with spatial coordinates, we employ the Leibnitz formula with the previous boundary conditions. This formula, which is valid for all integrable and derivable function $f(x, p)$ and for all interval $[a(x), b(x)]$ with boundaries varying with x, reads :

$$\begin{array}{c} \int_{a(x)}^{b(x)} \frac{\partial f(x,p)}{\partial x} dp = \\ \frac{\partial}{\partial x} \left(\int_{a(x)}^{b(x)} f(x,p) dp \right) - f(x, b(x)) \frac{\partial b(x)}{\partial x} + f(x, a(x)) \frac{\partial a(x)}{\partial x}. \end{array} \tag{27}$$

Thus, using Equation 26 and Equation 27, the vertical integration of Equation 24 in the pressure interval $[\tilde{p}(s^{k+1}), \tilde{p}(s^k)]$ yields to a momentum conservation equation for the k-th atmospheric layer :

$$\frac{\partial (\tilde{\mathbf{q}}^k)}{\partial t} + \mathrm{div}(\frac{1}{\tilde{h}^k} \tilde{\mathbf{q}}^k \otimes \tilde{\mathbf{q}}^k) + \frac{1}{2\overline{\rho}^k} \nabla_{xy} (\tilde{h}^k)^2 + \begin{bmatrix} 0 & -1 \\ 1 & 0 \end{bmatrix} f^\phi \tilde{\mathbf{q}}^k = \nu_{\mathcal{T}}^k \Delta(\tilde{\mathbf{q}}^k) \tag{28}$$

with

$$\tilde{h}^k = \tilde{p}(s^k) - \tilde{p}(s^{k+1}), \tag{29}$$

$$\tilde{\mathbf{v}}^k = (\tilde{u}^k, \tilde{v}^k) = \frac{1}{\tilde{h}^k} \int_{\tilde{p}(s^{k+1})}^{\tilde{p}(s^k)} \tilde{\mathbf{v}} dp, \tag{30}$$

$$\tilde{\mathbf{q}}^k = \tilde{h}^k \tilde{\mathbf{v}}^k, \tag{31}$$

$$\mathrm{div}(\frac{1}{\tilde{h}^k} \tilde{\mathbf{q}}^k \otimes \tilde{\mathbf{q}}^k) = \begin{bmatrix} \frac{\partial (\tilde{h}^k (\tilde{u}^k)^2)}{\partial x} + \frac{\partial (\tilde{h}^k \tilde{u}^k \tilde{v}^k)}{\partial y} \\ \frac{\partial (\tilde{h}^k \tilde{u}^k \tilde{v}^k)}{\partial x} + \frac{\partial (\tilde{h}^k (\tilde{v}^k)^2)}{\partial y} \end{bmatrix}, \tag{32}$$

By vertical integration of the continuity equation (Equation 25) in the pressure interval $[\tilde{p}(s^{k+1}), \tilde{p}(s^k)]$, we supplement the momentum conservation law of Equation 28 by the mass conservation law :

$$\frac{\partial \tilde{h}^k}{\partial t} + \mathrm{div}(\tilde{\mathbf{q}}^k) = 0, \tag{33}$$

and obtain independent shallow-water equation systems for atmospheric layers $k \in [1, K]$:

$$\begin{cases} \frac{\partial \tilde{h}^k}{\partial t} + \mathrm{div}(\tilde{\mathbf{q}}^k) = 0 \\ \frac{\partial (\tilde{\mathbf{q}}^k)}{\partial t} + \mathrm{div}(\frac{1}{\tilde{h}^k}\tilde{\mathbf{q}}^k \otimes \tilde{\mathbf{q}}^k) + \frac{1}{2\overline{p}^k}\nabla_{xy}(\tilde{h}^k)^2 + \begin{bmatrix} 0 & -1 \\ 1 & 0 \end{bmatrix} f^\phi \tilde{\mathbf{q}}^k \\ = \nu_{\mathcal{I}}^k \Delta(\tilde{\mathbf{q}}^k), \end{cases} \tag{34}$$

Note that as we are in the isobaric coordinate system, partial derivatives with respect to x, y and t are defined at constant pressure p. However, according to section 3, pressure difference observations correspond to rough constant pressure interval. Therefore, such data fit the shallow water model of Equation 34 defined in the isobaric coordinate system. Note that the proposed shallow-water system describes the dynamics of physical quantities expressed in standard units. Thus, some dimension factors appear in the equation when it is discretized on a pixel grid with velocities expressed in pixels per frame and pressure in hPa[1].

4.2 Estimation and tracking of wind and pressure fields

Let us now define the components of the assimilation system controlling the initial conditions used for the dense estimation and the tracking of pressure difference maps $\tilde{h}^k$ and average velocities $\tilde{\mathbf{v}}^k$ related to the set of $k \in [1, K]$ layers.

4.2.1 State variables

The state variable considered for each of the layers $k \in [1, K]$ is composed of the height and of the flow : $X^k = [\tilde{h}^k, \tilde{\mathbf{q}}^k]^T$. The control of the initial conditions $\tilde{h}^k(t_0)$ and $\tilde{\mathbf{q}}^k(t_0)$ of the system (34) is performed through the control variables η_h^k and $\eta_{\mathbf{q}}^k$:

$$\begin{cases} \tilde{h}^k(t_0) = \tilde{h}_0^k + \eta_h^k \\ \tilde{\mathbf{q}}^k(t_0) = \tilde{\mathbf{q}}_0^k + \eta_{\mathbf{q}}^k \end{cases} \tag{35}$$

4.2.2 Observation operator

Observations h_{obs}^k are provided by the pressure difference maps introduced in section 3.2. As we aim to track the filtered state vector $[\tilde{h}^k, \tilde{\mathbf{q}}^k]^T$ and as we

[1] As one pixel represents δp meters and one frame corresponds to Δt seconds, the densities $\overline{p}^k$ expressed in pascal by square seconds per square meter ($Pa\ s^2/m^2$) must be multiplied by $10^{-2}\delta p^2/\Delta t^2$, and Coriolis factor f^ϕ expressed per seconds must be multiplied by Δt. By a scale analysis and as also observed in our experiments, for $\Delta t = 900$ seconds, the third term of Equation 28 has a magnitude similar to other terms if $\delta x \sim 100$. This is in agreement with the shallow water assumption.

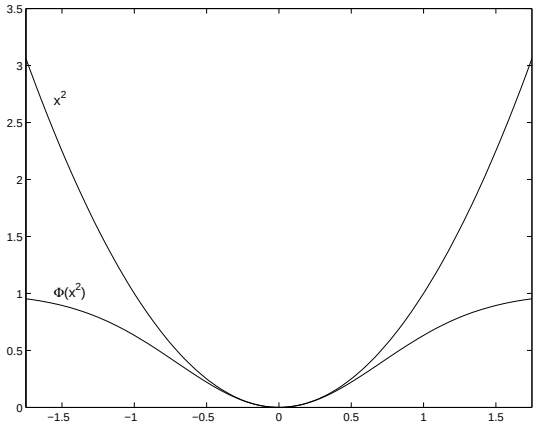

Figure 2: Graph of a robust cost function ($\Phi(x^2) = 1 - exp(\frac{x^2}{\sigma^2})$) compared to a quadratic function.

only observe non filtered h^k_{obs}, the observation system $\boldsymbol{\mathcal{Y}} = \mathbb{H}(X)$ is thus simply defined by :

$$\left\{ \begin{array}{ll} \boldsymbol{\mathcal{Y}} & = \tilde{h}^k_{obs} = K_{\delta_x} * h^k_{obs} \\ \mathbb{H} & = [I_d, 0] \end{array} \right. . \tag{36}$$

This means that the motion correction will be achieved relying uniquely on pressure difference observations.

4.2.3 Cost function

Assuming those variables are of weak energy yields to the minimization of the following functional for layer k :

$$J_k(\eta^k_h, \eta^k_{\mathbf{q}}) = \frac{1}{2} \int_{t_0}^{t_f} \phi \left(\| K_{\delta_x} * h^k_{obs} - \tilde{h}^k(\eta^k_h, \eta^k_{\mathbf{q}}) \|^2_{R^k} \right) dt + \frac{1}{2} \| \eta^k_h \|^2_{B^k_h} + \frac{1}{2} \| \eta_{\mathbf{q}^k} \|^2_{B^k_{\mathbf{q}}}, \tag{37}$$

where B^k_h and $B^k_{\mathbf{q}}$ denote the covariance matrices associated to the initial control functions η_h and $\eta_{\mathbf{q}^k}$. A robust penalty function $\phi(.)$ has been introduced in the previous functional to remove unreliable observations, that is to say observations which constitute outliers for the shallow-water model. Such cost functions penalizes large "residual" values less drastically than quadratic functions do [15, 11, 26], as illustrated in figure 2. It can be shown, under certain simple conditions (mainly concavity of $\Phi(\sqrt{x})$), that any multidimensional minimization problem of the form

$$\arg\min_X \int \phi(g(X)^2) d\boldsymbol{x}, \tag{38}$$

can be turned into a dual minimization problem:

$$\arg\min_{X,z} \int [zg(X)^2 + \psi(z)]d\boldsymbol{x}. \tag{39}$$

This new optimization problem involves an additional *auxiliary variable* (or *weight* function) $z(\boldsymbol{x})$ with value in the range $[0, 1]$. Function ψ is a continuously differentiable function defined from ϕ and that is uniquely a function of the weight variables. The new minimization is then lead *alternatively* with respect to X and to z. If g is an affine function, minimization w.r.t. X is a standard *weighted least squares* problem. The variable X being frozen, it can be shown that the best weights have the following closed form [11]:

$$\hat{z}(\boldsymbol{x}) = \phi'[g(X(\boldsymbol{x}))^2]. \tag{40}$$

Experimentally the use of these functions has proven to bring significant improvements for computer vision application. In this work, a Leclerc M-estimator has been chosen for $\phi(x^2) = 1 - \exp\frac{-x^2}{\sigma^2}$. In practice at each update of the state variables, the new optimal value of the weight variable $\hat{z}(\boldsymbol{x}) = \exp\frac{-x^2}{\sigma^2}$ is computed and a new weighted quadratic norm is considered in the assimilation process. This norm reads $\|\cdot\|^2_{Z^k R^k}$ where Z^k is the outlier diagonal matrix defined as

$$Z^k(\mathbf{x}, \mathbf{x}') = \begin{cases} \exp\frac{-g(X(\mathbf{x}))^2}{\sigma^2}, \text{if} \quad \mathbf{x} = \mathbf{x}' \\ 0 \text{ else.} \end{cases} \tag{41}$$

4.2.4 Dynamical operator

The dynamical model $\mathbb{M}(\tilde{h}^k, \tilde{\mathbf{q}}^k)$ is given by Equation 34. The adjoint operator of a shallow-water equation system can be expressed analytically [17]. For the dynamical model defined in Equation 34, the adjoint operator $(\partial_{X^k}\mathbb{M})^*$ associated with the adjoint variable $\lambda^k = [\lambda_h^k, \lambda_{\mathbf{q}}^k]^T$ reads :

$$\begin{cases} -\partial_t \lambda_h^k + \tilde{\mathbf{v}}^k \cdot (\tilde{\mathbf{v}}^k \cdot \nabla)\lambda_{\mathbf{q}}^k - \frac{\tilde{h}^k}{\varrho^k}\text{div}(\lambda_{\mathbf{q}}^k) = (R^k)^{-1}(K_{\delta_x} * \tilde{h}_{obs}^k - \tilde{h}^k), \\ -\partial_t \lambda_{\mathbf{q}}^k - (\tilde{\mathbf{v}}^k \cdot \nabla)\lambda_{\mathbf{q}}^k - (\nabla\lambda_{\mathbf{q}}^k)\tilde{\mathbf{v}}^k - \nabla\lambda_h^k + \begin{bmatrix} 0 & 1 \\ -1 & 0 \end{bmatrix} f^\phi \lambda_{\mathbf{q}}^k = \nu_T^k \Delta(\lambda_{\mathbf{q}}^k), \\ \lambda_h^k(t_f) = 0, \\ \lambda_{\mathbf{q}}^k(t_f) = 0, \end{cases} \tag{42}$$

where λ_h^k and $\lambda_{\mathbf{q}}^k$ denote the two components of the adjoint variable λ^k related to layer k. Let us remark that the turbulent viscosity has been considered as being given by the direct integration. Its value is maintained in the backward integration. More details on the construction of adjoint models can be found in [36].

The implementation of bi-dimensional advection systems can be quite complex. We chose for the spatial discretization of the shallow water Equation 34 the non oscillatory schemes proposed in [39]. The temporal integration is achieved with a third order Runge-Kutta scheme and a time step dt which respects the total variation diminishing property [19].

4.2.5 Covariance matrices and initialization issues

An inverse diagonal covariance matrix $(R^k)^{-1}$ is directly defined using the mask of observation C^k :

$$(R^k)^{-1}(\mathbf{s},\mathbf{s}) = \begin{cases} \alpha_{obs} & \text{if} \quad \mathbf{s} \in C^k \\ 0 & \text{else,} \end{cases} \tag{43}$$

where α_{obs} is a fixed parameter defining the inverse of the observation covariances. In an analogous way inverse diagonal covariance matrices $(B_h^k)^{-1}$ and $(B_{\mathbf{q}}^k)^{-1}$ are defined as :

$$\begin{cases} (B_h^k)^{-1}(\mathbf{s},\mathbf{s}) = \alpha_h \\ (B_{\mathbf{q}}^k)^{-1}(\mathbf{s},\mathbf{s}) = \alpha_{\mathbf{q}} \end{cases} \tag{44}$$

where α_h and $\alpha_{\mathbf{q}}$ are fixed parameters defining the inverse of the initial variable covariances.
However, as observations are sparse and noisy, nine-diagonal inverse covariance matrices obtained by Gaussian smoothing are employed to diffuse information in the 3x3 vicinity of any pixel supporting observations.

As no guaranty of convergence towards a global minimum can be insured for such a non-convex functional, the quality of results depends on the initial conditions given to the system. We chose to initialize the state variables $\tilde{h}_0^k$ with a constant height computed as the average height observed on the layer. Initial velocity fields $\tilde{\mathbf{v}}_0^k$ are provided by an optic-flow algorithm dedicated to atmospheric layers [14]. These two elements provide the initial state variable $\tilde{\mathbf{q}}_0^k = \tilde{h}_0^k \tilde{\mathbf{v}}_0^k$.

5 Image assimilation with an imperfect dynamical model

In order to relax the layering assumption, we describe the evolution of the filtered state variables using a simplified version of the previously introduced shallow-water equations and perform assimilation using an imperfect modeling scheme. Moreover, we propose to use an image-adapted observation operator, able to exploit the fine spatio-temporal image structures, but at the same time, remain related to the spatially filtered state variables.

5.1 Simplified filtered vorticity-divergence model

In order to simplify Equation 34, we assumed filtered horizontal motion components to be homogeneous within the layer. In other words, we neglect their vertical derivatives and consider that filtered horizontal winds $\tilde{\mathbf{v}}^k$ which have been vertically averaged are equal to filtered horizontal winds on layer upper surfaces $\mathbf{s}^{k+1}$. Using such an assumption yields :

$$\tilde{\mathbf{v}}_t^k + \boldsymbol{\nabla}(\tilde{\mathbf{v}}^k)\tilde{\mathbf{v}}^k - \rho_0^{-1}\nabla\tilde{p}(s^{k+1}) + \begin{bmatrix} 0 & -1 \\ 1 & 0 \end{bmatrix} f^{\phi}\tilde{\mathbf{v}}^k = \nu_T \boldsymbol{\Delta}(\tilde{\mathbf{v}}^{\mathbf{k}}) \tag{45}$$

with the notations $\boldsymbol{\nabla}(\tilde{\mathbf{v}}^{\mathbf{k}}) = (\nabla\tilde{u}^k, \nabla\tilde{v}^k)^\top$ and $\boldsymbol{\Delta}(\tilde{\mathbf{v}}^{\mathbf{k}}) = (\Delta\tilde{u}^k, \Delta\tilde{v}^k)^\top$. Let us denote the vorticity by $\tilde{\zeta}^k = \mathrm{curl}(\tilde{\mathbf{v}}^k)$ and the divergence by $\tilde{D}^k = \mathrm{div}(\tilde{\mathbf{v}}^k)$. The previous system may be expressed in its vorticity-divergence form :

$$\left\{ \begin{array}{l} \tilde{\zeta}^k_t + \tilde{\mathbf{v}}^k \cdot \nabla\tilde{\zeta}^k + (\tilde{\zeta}^k + f^\phi)\tilde{D}^k = \nu_{\mathcal{T}}\Delta(\tilde{\zeta}^k) \\ \tilde{D}^k_t + \tilde{\mathbf{v}}^k \cdot \nabla\tilde{D}^k + (\tilde{D}^k)^2 - 2|J| - \rho_0^{-1}\Delta\tilde{p}(s^{k+1}) + f^\phi\tilde{\zeta}^k = \nu_{\mathcal{T}}\Delta(\tilde{D}^k) \end{array} \right. \tag{46}$$

where $|J|$ is the determinant of the Jacobian matrix of variables $(\tilde{u}^k, \tilde{v}^k)$. For vorticity based large eddy simulation formulations, we may rely on enstrophy-based sub-grid models, instead of using the Smagorinsky model (Equation 23). Such models are based on Taylor's vorticity transfer and dissipation by small scales theory [37]. Consequently, the sub-grid turbulent dissipation term in the curl transport equation may be modeled by the enstrophy-based sub-grid model proposed in [25]. Such a model reads :

$$\nu_{\mathcal{T}} = (C\delta_x)^2|\tilde{\zeta}^k|. \tag{47}$$

In the momentum conservation formulations of Equation 45 and Equation 46, dynamical models predict the evolution of velocity components $(\tilde{u}^k, \tilde{v}^k)$ and of divergence and vorticity $(\tilde{\zeta}^k, \tilde{D}^k)$. In both models, one of the major difficulties is induced by the dependence to the pressure variable $\tilde{p}(s^{k+1})$ which is an unknown variable of the k-th layer state. Adding pressure as a new state variable in the assimilation process, whose evolution can be described by the mass conservation law of Equation 33 constitutes a solution for achieving the model integrations. However, we will need to later employ latter this mass conservation law to define the observation operator. Thus, we search instead to derive a dynamical model which is independent of the pressure unknown. In opposition to the classical formulation, the vorticity-divergence equations have the advantage of providing a dynamical model for which the vorticity evolution is independent of pressure. Concerning the divergence, as at large scales it can be considered weak almost everywhere, we will rely on an approximate evolution law.

We assume here that the divergence is advected by the flow and a noise variable that encodes the uncertainty on the model. More precisely we will assume that the divergence map is a function of a stochastic process representing a particle position and is driven by the folowing stochastic differential equation:

$$d\mathbf{x}(t) = \tilde{\mathbf{v}}^k(\mathbf{x}(t))dt + \sqrt{2\nu_T}dB(t). \tag{48}$$

This equation states that the particle position is known only up to an uncertainty that grows linearly with time. B_t is a standard Brownian motion of $\mathbb{R}^2$. The process $\mathbf{x}_t$ starts at points, $\boldsymbol{x}_o$. It can be shown through the Ito formula and Kolmogorov's forward equation, that the expectation at time t of such a function, $\xi(t, \mathbf{x}) = \mathbb{E}[\mathrm{div}\tilde{\mathbf{v}}^k(\mathbf{x}(t))]$ obeys an advection diffusion equation [27]:

$$\begin{array}{l} \xi_t + \tilde{\mathbf{v}}^k \cdot \nabla\xi + \xi\mathrm{div}\tilde{\mathbf{v}}^k - \nu_T\Delta\xi = 0, \\ \xi(0, \boldsymbol{x}_0) = \mathrm{div}\tilde{\mathbf{v}}^k(\boldsymbol{x}_0). \end{array} \tag{49}$$

Assuming that the divergence of the flow is given by its expectation ($\tilde{D}^k \approx \xi$) allows us to write the simplified filtered vorticity-divergence model for the layer k as:

$$\left\{ \begin{array}{l} \tilde{\zeta}^k_t + \tilde{\mathbf{v}}^k \cdot \nabla \tilde{\zeta}^k + (\tilde{\zeta}^k + f^\phi)\tilde{D}^k = \nu_{\mathcal{T}} \Delta \tilde{\zeta}^k \\ \tilde{D}^k_t + \tilde{\mathbf{v}}^k \cdot \nabla \tilde{D}^k + (\tilde{D}^k)^2 = \nu_{\mathcal{T}} \Delta \tilde{D}^k \end{array} \right. . \tag{50}$$

In this model we assume that the divergence of the flow is weak and is similar to the divergence expectation. The divergence equation does not describe anymore the evolution of the flow divergence but the evolution of its expectation. The expectation of the divergence value is advected by the flow and dissipates due to a subgrid isotropic incertitude. This hypothesis is quite natural in large scale modeling.

5.2 Estimation and tracking of filtered wind fields

In this section, we present all components required to estimate and track the wind fields with an assimilation scheme using an imperfect model.

5.2.1 Cost function and state variables

We choose to represent the system state (*i.e.* the velocity field) through the curl and divergence components as their evolution can be described by Equation 50 and as they completely determine the underlying 2D velocity up to a laminar flow. Indeed, denoting the orthogonal gradient by $\nabla^\perp = (-\partial/\partial y, \partial/\partial x)^\top$ and the 2D Green kernel G associated with the Laplacian operator, the Helmholtz decomposition of the field can be expressed as :

$$\tilde{\mathbf{v}}^k = \underbrace{\nabla^\perp (G * \tilde{\zeta}^k)}_{\tilde{\mathbf{v}}^k_{sol}} + \underbrace{\nabla (G * \tilde{D}^k)}_{\tilde{\mathbf{v}}^k_{irr}} + \tilde{\mathbf{v}}^k_{har}, \tag{51}$$

where $\tilde{\mathbf{v}}^k_{har}$ is an harmonic transportation part ($div \tilde{\mathbf{v}}^k_{har} = \text{curl} \tilde{\mathbf{v}}^k_{har} = 0$). In our applications, we assume that this component of the velocity is constant. This component may be recovered by subtracting its solenoidal and irrotationnal parts from the initial field $\tilde{\mathbf{v}}^k_0$. As a consequence, the field can be represented by its div-curl components as :

$$\tilde{\mathbf{v}}^k = \nabla^\perp (G * \tilde{\zeta}^k) + \nabla (G * \tilde{D}^k) = \underbrace{\left[\nabla^\perp G *, \nabla G * \right]}_{\mathbb{H}_G} \left[\begin{array}{c} \tilde{\zeta}^k \\ \tilde{D}^k \end{array} \right] \tag{52}$$

where the operator $\mathbb{H}_G$ can efficiently be computed in the Fourier domain.

As the divergence-vorticity model constitutes only an approximate dynamical system describing atmospheric layer evolution, we employ the assimilation scheme derived for imperfect models which has been presented in section 2.2. This yields the minimization of the functional introduced in Equation 7 and Equation 6 with the dynamical and observation operators defined in the following.

5.2.2 Dynamical operator

The dynamical model required for the assimilation in (6) is defined by relation (50). This model is associated with an imperfect dynamical modeling where

the model errors are here related to Coriolis effect, to the pressure difference dissipation on the divergence component and to the sub-grid stress tensor error on the vorticity and divergence component.

The associated tangent linear system (Equation 14) around the current solution $X^\star = [\tilde{\zeta}^\star, \tilde{D}^\star]^T$ is:

$$\begin{aligned} \partial_t \begin{bmatrix} \tilde{\zeta}^k \\ \tilde{D}^k \end{bmatrix} + \underbrace{\begin{bmatrix} \tilde{\mathbf{v}}^\star \cdot \nabla + \tilde{D}^\star - \nu_{\mathcal{T}} \Delta & \tilde{\zeta}^\star + f^\phi \\ 0 & \tilde{\mathbf{v}}^\star \cdot \nabla + \tilde{D}^\star - \nu_{\mathcal{T}} \Delta \end{bmatrix}}_{\partial_{X^\star} \mathbb{M}} \begin{bmatrix} \tilde{\zeta}^k \\ \tilde{D}^k \end{bmatrix} \\ = Q^k \lambda, \end{aligned} \tag{53}$$

where $\nu_{\mathcal{T}} = (C\delta_x)^2 |\tilde{\zeta}^\star|$ and with the covariance matrix Q^k which will be defined in section 5.2.4. At each time increment dt, the current velocity solution $\tilde{\mathbf{v}}^\star$ is updated according to vorticity $\tilde{\zeta}^k$, divergence $\tilde{D}^k$ and harmonic transportation $\tilde{\mathbf{v}}^k_{har}$ using operator defined in Equation 52. The adjoint variables $[\lambda^k_\zeta, \lambda^k_D]^T$ are obtained with the following adjoint system:

$$\left\{ \begin{array}{l} \lambda^k_\zeta(t_f) = 0, \\ \lambda^k_D(t_f) = 0, \\ -\partial_t \begin{bmatrix} \lambda^k_\zeta \\ \lambda^k_D \end{bmatrix} + \underbrace{\begin{bmatrix} -\tilde{\mathbf{v}}^\star \cdot \nabla + \tilde{D}^\star - \nu_{\mathcal{T}} \Delta & \tilde{\zeta}^\star + f^\phi \\ 0 & -\tilde{\mathbf{v}}^\star \cdot \nabla + \tilde{D}^\star - \nu_{\mathcal{T}} \Delta \end{bmatrix}}_{(\partial_{X^\star} \mathbb{M})^*} \begin{bmatrix} \lambda^k_\zeta \\ \lambda^k_D \end{bmatrix} \\ = \partial_{X^k} \mathbb{H}^* R^{-1} (Y - \mathbb{H}(X)). \end{array} \right. \tag{54}$$

Let us remark that the turbulent viscosity $\nu_{\mathcal{T}}$ and the velocity $\tilde{\mathbf{v}}^\star$ are computed during the direct integration and maintained in the backward integration. As opposed to the traditional shallow water setting, the resulting adjoint equation includes a turbulent viscosity. Discretization of this dynamical model has been achieved using spatial and temporal schemes similar to those used previously. The observation errors $Y - \mathbb{H}(X)$ and the covariance matrix R are defined in the next sections.

5.2.3 Observation operator

The mass conservation law of Equation 33 is used to define our observation operator:

$$\frac{\partial h^k_{obs}(\mathbf{s}, t)}{\partial t} + \nabla h^k_{obs}(\mathbf{s}, t) \cdot \tilde{\mathbf{v}}^k(\mathbf{s}, t) + h^k_{obs}(\mathbf{s}, t) \mathrm{div} \tilde{\mathbf{v}}^k(\mathbf{s}, t) \approx 0, \tag{55}$$

However, this formulation can not be used alone, as it provides only one equation for two unknowns at each spatio-temporal location $(\mathbf{s}, t)$, with therefore a one dimensional family of solutions in general. To remove such ambiguities, a common approach consists in assuming a spatial coherence of wind field estimates in a given neighborhood (similar to the well-known approach of [24] used in computer vision). In the present case, this assumption is valid since unknowns are filtered velocity vectors $\tilde{\mathbf{v}}^k(\mathbf{s}, t)$ spatially coherent at a location $\mathbf{s}$ within a neighborhood of size δ_x. Therefore, the motion field can be measured through the relation (omitting the spatio-temporal indexes $(\mathbf{s}, t)$ for sake of clarity):

$$K_{\delta_x} * \left(\frac{\partial h^k_{obs}}{\partial t} + \nabla h^k_{obs} \cdot \tilde{\mathbf{v}} + h^k_{obs} \mathrm{div} \tilde{\mathbf{v}}^k \right) \approx 0, \tag{56}$$

where K_{δ_x} is a Gaussian kernel of size δ_x. From the previous relation and recalling that $\tilde{\mathbf{v}}^k = \mathbb{H}_G X$ (with $X = [\tilde{\zeta}^k, \tilde{D}^k]^T$), one can easily define our observation system $\boldsymbol{\mathcal{Y}} = \mathbb{H}(X)$ with:

$$\left\{ \begin{array}{ll} \boldsymbol{\mathcal{Y}} & = K_{\delta_x} * \frac{\partial h^k_{obs}(\mathbf{s},t)}{\partial t} \\ \mathbb{H} & = -\left(K_{\delta_x} * \nabla h^k_{obs}\right)^T \mathbb{H}_G - \left(K_{\delta_x} * h^k_{obs}\right) \nabla^T \mathbb{H}_G \end{array} \right. . \tag{57}$$

The observation operator $\mathbb{H}$ is linear w.r.t the state variable $X = [\tilde{\zeta}^k, \tilde{D}^k]^T$ and is then identical to its linear tangent operator. Noting that the adjoint of $\mathbb{H}_G$ is $-\mathbb{H}_G$ (as shown in [29]), the adjoint of $\mathbb{H}$ therefore reads :

$$\partial_{X^\star} \mathbb{H}^* = \mathbb{H}_G \left(K_{\delta_x} * \nabla h^k_{obs} \right) - \left(K_{\delta_x} * h^k_{obs} \right) \mathbb{H}_G \nabla. \tag{58}$$

5.2.4 Covariance matrices and initialization issues

Nine-diagonal inverse covarianc matrices $(B^k_{\tilde{\mathbf{v}}})^{-1}$ and $(R^k)^{-1}$ fixing the inaccuracy of the initial condition $\tilde{\mathbf{v}}^k_0$ and of observations h^k_{obs} have been defined similarly to section 4.2.5. Moreover, a nine-diagonal inverse covariance matrix $(Q^k)^{-1}$ fixing the model inaccuracy with a given parameter α_Q has been defined analogously.

Initial velocities $\tilde{\mathbf{v}}^k_0$ are obtain by filtering wind fields, provided by the optic-flow algorithm dedicated to atmospheric layers proposed in [14], with the Gaussian Kernel K_{δ_x}.

6 Experiments

6.1 Synthetic image sequence

For numerical evaluation of the image assimilation schemes, we have relied on synthetic image observations generated by short time numerical simulation of atmospheric layer motion. As the two assimilation schemes proposed in this paper rely on different dynamical models, we derived two different benchmarks according to a perfect and an imperfect shallow-water modeling given respectively by Equation 34 and Equation 50. For both cases, we chose a realistic initial condition on motion (and on layer pressure difference for Equation 34) to integrate the models in an equivalent time period of 2h30min and create two different sequence benchmarks composed of 10 images each which were denoted respectively by *seq-a* (for the perfect model) and *seq-b* (for the imperfect model) . Each image is composed of 128×128 pixels and represent a spatial area of approximatively $400 km^2$. These benchmarks have then been deteriorated by different noises and by masking operations; we formed 4 synthetic sequences a_1, a_2, a_3, a_4 related to *seq-a*, and 4 other synthetic sequences b_1, b_2, b_3, b_4 related to *seq-b*. Sequences a_1, b_1 and a_2, b_2 were composed of dense observations of h^k_{obs} in hPa, corrupted by Gaussian noises with standard deviation respectively

Exp.	Mask	Noise %	$\tilde{h}^k_{obs}(t_0)$ RMSE (hPa)	$\lvert\tilde{\mathbf{v}}^k(t_0)\rvert$ RMSE (pixel/frame)	$\lvert\tilde{\mathbf{v}}^k(t)\rvert$ RMSE (pixel/frame)
a_1	no	15	28.79	0.0932	0.0911
a_2	no	30	57.85	0.1869	0.1828
a_3	yes	15	25.42	0.0932	0.0915
a_4	yes	30	58.28	0.1836	0.1822

Figure 3: **Initial setup used for assimilation with a perfect model**. Initial Root Mean Square Error (RMSE) on observations $\tilde{h}^k_{obs}$ at initial time t_0 and on wind norm $|\tilde{\mathbf{v}}^k|$ at initial time t_0 or at all times t of the image synthetic sequences.

Exp.	final RMSE on $\tilde{h}^k(t_0)$(hPa)	final RMSE on $\lvert\tilde{\mathbf{v}}^k(t_0)\rvert$(pixel/frame)	final RMSE on $\lvert\tilde{\mathbf{v}}^k(t)\rvert$ (pixel/frame)
a_1	3.1100	0.0120	0.0128
a_2	5.0421	0.0150	0.0153
a_3	4.0808	0.0128	0.0135
a_4	5.3249	0.0166	0.0168

Figure 4: **Final estimation errors obtained by assimilation with a perfect model**. RMSE on estimates $\tilde{h}^k$ and $|\tilde{\mathbf{v}}^k|$ at initial time t_0 or at all times t of the image synthetic sequences.

equal to 15% and 30% of the pressure amplitude. A realistic cloud classification sequence was employed to extract regions from a_1, a_2, b_1 and b_2 in order to create noisy and incomplete synthetic sequences a_3, a_4, b_3 and b_4. For initializing the assimilation systems, we have used the synthetic ground truth values of variables $\tilde{h}^k(t_0)$ and $\tilde{\mathbf{v}}^k(t_0)$ deteriorated by Gaussian noises with standard deviation equal to 15% and 30% of the variable amplitudes respectively for experiments using synthetic sequences a_1, a_3, b_1, b_3 and a_2, a_4, b_2, b_4.

Table 3 and table 7 summarize the initial setup used for numerical evaluation of the two assimilation schemes. Furthermore, these tables present the Root Mean Square Error (RMSE) before assimilation of state variables. Figure 5 and figure 9 displays examples of noisy and sparse pressure difference observations and initial values of the state variables used in the experiments.

6.1.1 Perfect scheme

Comparing table 3 and table 4, one can notice significant decreases induced by the assimilation system on the RMSE between real and estimated velocities and pressure; the final RMSE reduces roughly by a factor of 10 with the assimilation process. Moreover, the stable behavior of the RMSE on motion fields and reconstructed pressure maps in these tables demonstrates the robustness of the approach when dealing with incomplete and noisy observations. Reconstruction of pressure maps and estimation of motion fields for experiments a_2 and a_3 are presented in figure 6. A comparison with images of variable initial states displayed in figure 5 clearly illustrates the estimation efficiency.

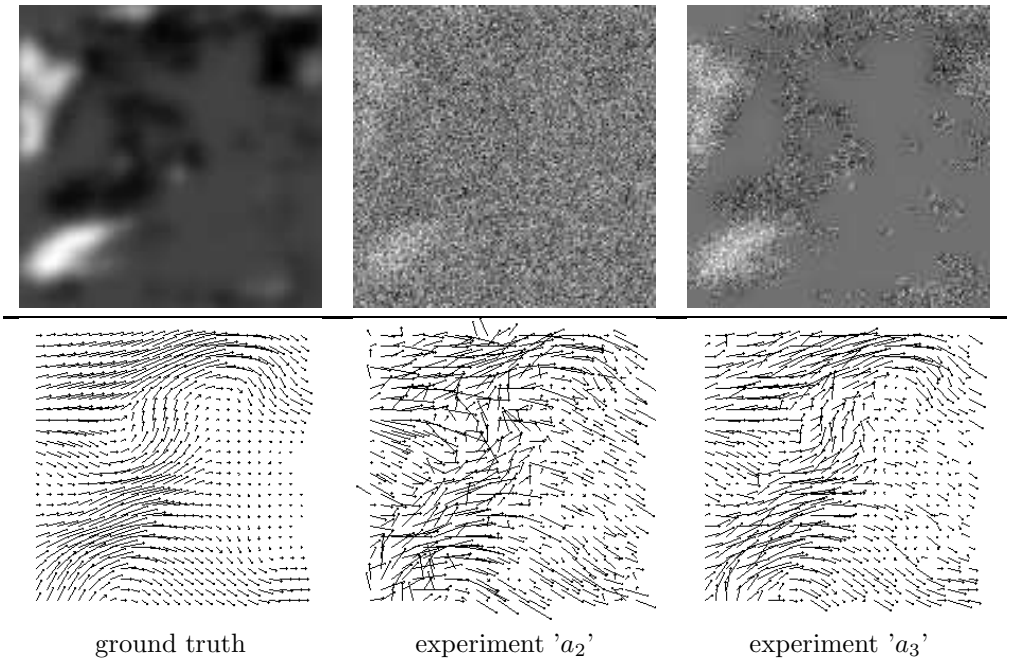

ground truth experiment 'a_2' experiment 'a_3'

Figure 5: **Observations and state variables before assimilation with a perfect model** : $\tilde{h}^k_{obs}(t_0)$ (first line) and $\tilde{\mathbf{v}}^k(t_0)$ (second line) at initial time.

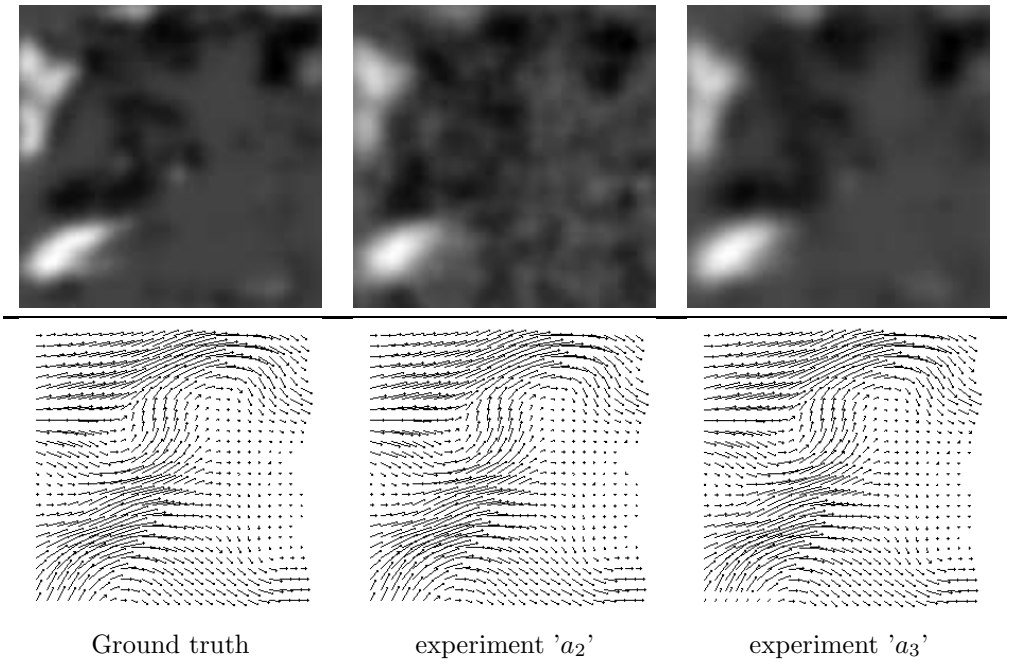

Ground truth experiment 'a_2' experiment 'a_3'

Figure 6: **Variables after assimilation with a perfect model**: pressure difference $\tilde{h}^k(t_0)$ (first line) and wind fields $\tilde{\mathbf{v}}^k(t_0)$ (second line) estimates at initial time.

	Mask	Noise %	RMSE on $\tilde{\zeta}^k(t)$ (1/frame)	RMSE on $\tilde{D}^k(t)$ (1/frame)	RMSE on $\|\tilde{\mathbf{v}}^k(t)\|$ (pixel/frame)
b_1	no	20	0.0178	0.0305	0.0921
b_2	no	40	0.0265	0.0534	0.1003
b_3	yes	20	0.0179	0.0305	0.0925
b_4	yes	40	0.0265	0.0543	0.1152

Figure 7: **Initial setup used for assimilation with an imperfect model**. Root Mean Square Error (RMSE) on observations h^k_{obs}, on initial vorticity $|\tilde{\zeta}^k|$, divergence $|\tilde{D}^k|$ and wind norm $|\tilde{\mathbf{v}}^k|$ obtained at all times t of the image synthetic sequences.

	RMSE on $\tilde{\zeta}^k(t)$ (1/frame)	RMSE on $\tilde{D}^k(t)$ (1/frame)	RMSE on $\|\tilde{\mathbf{v}}^k(t)\|$ (pixel/frame)
b_1	0.0031	0.0017	0.0175
b_2	0.0048	0.0023	0.0216
b_3	0.0039	0.0019	0.0182
b_4	0.0049	0.0024	0.0233

Figure 8: **Final estimation errors obtained by assimilation with an imperfect model**. RMSE on estimates $\tilde{\zeta}^k(t)$, $\tilde{D}^k(t)$ and $|\mathbf{v}^k(t)|$ obtained at all times t of the image synthetic sequences.

6.1.2 Imperfect scheme

By comparison of values in table 7 and table 8, here again one can notice a significant decreases induced by the assimilation system on the RMSE between real and estimated velocities : the final RMSE reduces roughly by a factor of 5 with the assimilation process. Although the error reduction is still important, this is not as good as results obtained with an assimilation approach based on a perfect model. Here again, the stable behavior of the RMSE on vorticity, divergence and motion fields in these tables demonstrate the robustness of the approach when dealing with incomplete and noisy observations. Vorticity, divergence and motion fields estimates for experiments b_2 and b_3 are presented in figure 10. A comparison with images of variable initial states displayed in figure 9 clearly illustrates the estimation efficiency.

Although in these synthetic cases, the performance of a perfect modeling approach proved to overcome the performance of an imperfect modeling approach, one should moderate such a conclusion in real cases.

6.2 METEOSAT Satellite image sequence

We then turned to qualitative evaluations of METEOSAT Second Generation (MSG) meteorological image sequences acquired at a rate of an image every 15 minutes. This benchmark data, which has been provided by the EUMETSAT consortium, is composed of 10 images of top of cloud pressure and cloud-classification images. The image spatial resolution is 3×3 km^2 at the center of the whole Earth image disk. The cloud-classifications were used to segment

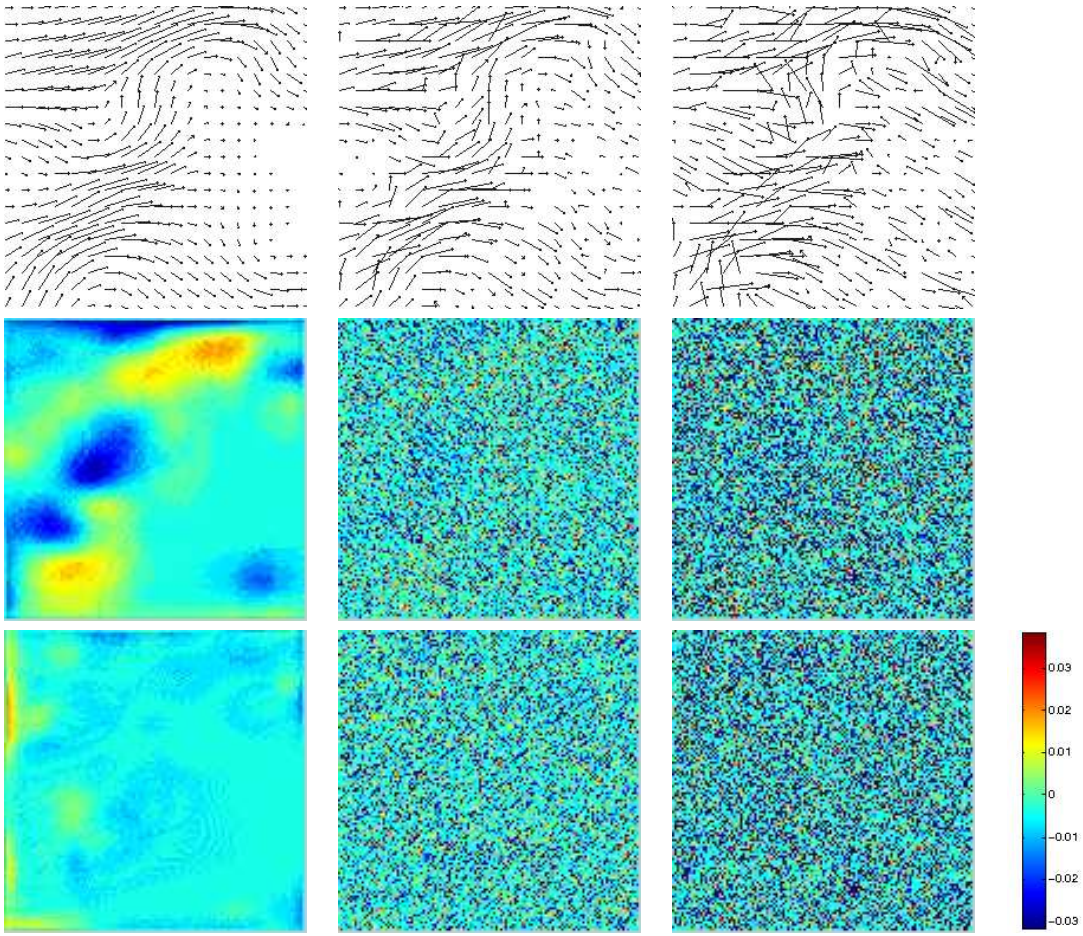

Ground truth experiment 'b_2' experiment 'b_3'

Figure 9: **State variables before assimilation with an imperfect model :** initial wind $\tilde{\mathbf{v}}^k$ (first line), vorticity $\tilde{\zeta}^k$ (second line) and divergence $\tilde{D}^k$ (third line) at initial time.

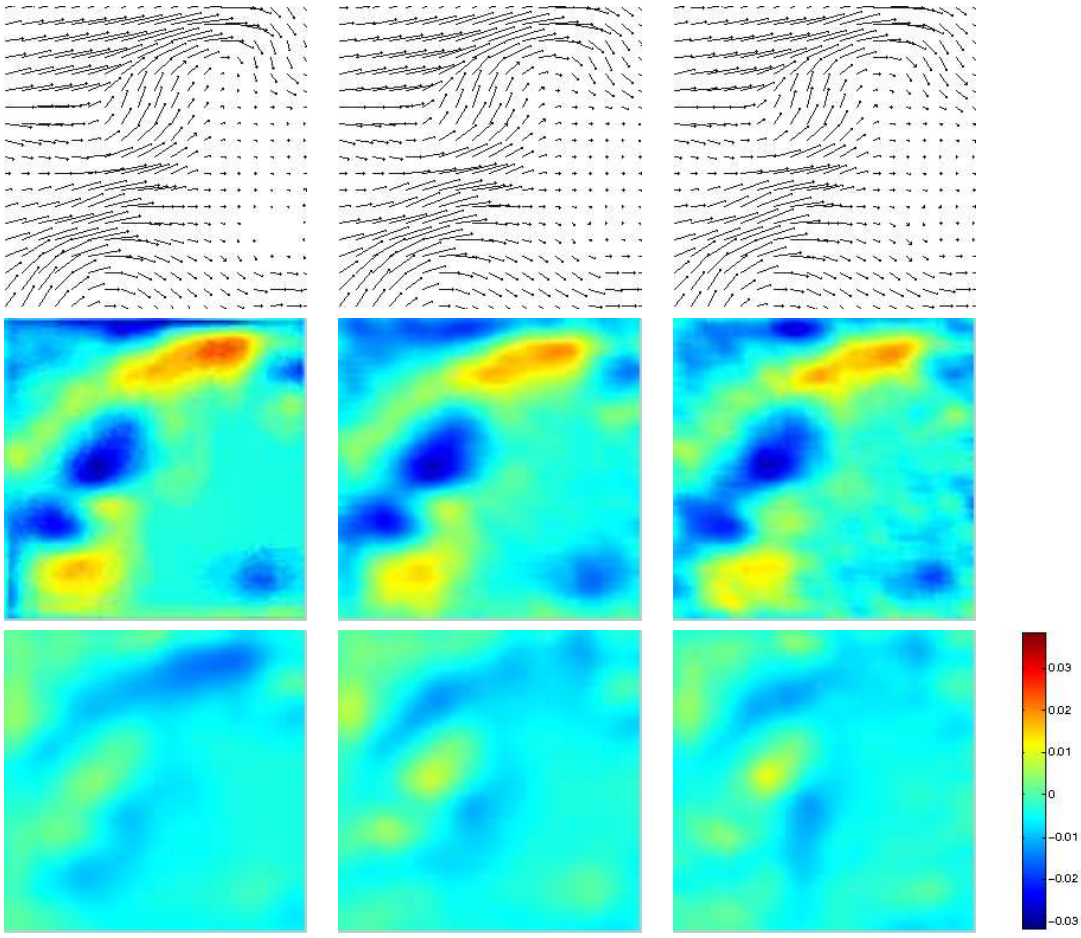

Ground truth | experiment 'b_2' | experiment 'b_3'

Figure 10: **Variables after assimilation with an imperfect model :** Wind $\tilde{\mathbf{v}}^k$ (first line), vorticity $\tilde{\zeta}^k$ (second line) and divergence $\tilde{D}^k$ (third line) fields at t= 1h15min

images into $K = 3$ broad layers, at low, intermediate and high altitude. Applying the methodology described in section 3, pressure difference images for the 3 layers were derived from pressure images. The sequence is composed of 10 images of 1024 x 1024 pixels covering an area over the north Atlantic Ocean (of about 3000 km^2) during part of one day (5-June-2004), from 12h00 to 14h30 UTC. (Coordinated Universal Time)

6.2.1 Perfect scheme

By assimilation of image observations with a perfect model, average motion and pressure difference maps are estimated from the image sequence for these 3 layers. In figure 11, reconstructed pressure difference maps can be compared to original and filtered pressure difference observations. Estimated vector fields superimposed on reconstructed pressure difference maps are displayed in figure 12 for each of the 3 layers. The motion fields estimated from the different layers on the cloudy observable parts are consistent with the visual inspection of the sequence. In particular, several motion differences between layers are very relevant. For instance, near the bottom left corner of the images, the lower layer possesses a southward motion while the intermediate layer moves northward.

Let us note that the assimilation scheme using a perfect model is limited to the estimation of large scale motion of layered atmospheric systems respecting the shallow water assumption. In some real cases, we noted that the term $\frac{1}{2\overline{\rho}^k}\nabla(\tilde{h}^k)^2$ of Equation 34 can locally dominate in areas where this assumption breaks, which results in local instabilities. To avoid such phenomena, we constrained in such cases the shallow water assumption to remain in force by increasing the filtering parameter δ_x up to a value above $100\delta_p^{-1}$ in order to consider scales greater than 100 km. The effect on observations of this filtering operation can be seen in figure 11. It results in a good characterization of large scale structure but also in a loss of information at small scales. This can be noticed in figure 13 which is a visual comparison between the lower layer motion component estimated by the layer-dedicated optic-flow method of [14] and by the proposed perfect model assimilation system. Indeed, time-persistent large structures of the flow are accurately estimated by both methods while noise and time-inconsistent structures have been removed only by the assimilation approach. However, smaller time-consistent structures have also been removed.

6.3 Imperfect scheme

Assimilation using an imperfect modeling scheme was then performed on the same image sequence. Motion fields estimated for the different layers are presented in figures 15 and 15 together with original observations. The motion fields estimated for the different layers are consistent with the results obtained by the previous method. Furthermore, smaller structures have been accurately characterized by this assimilation scheme. The enhancement at small scales can be noticed in figure 16. The vorticity and divergence estimates displayed in this figure can be compared to previous results displayed in figure 13. These small structures appear to be coherent with the reference optical flow results.

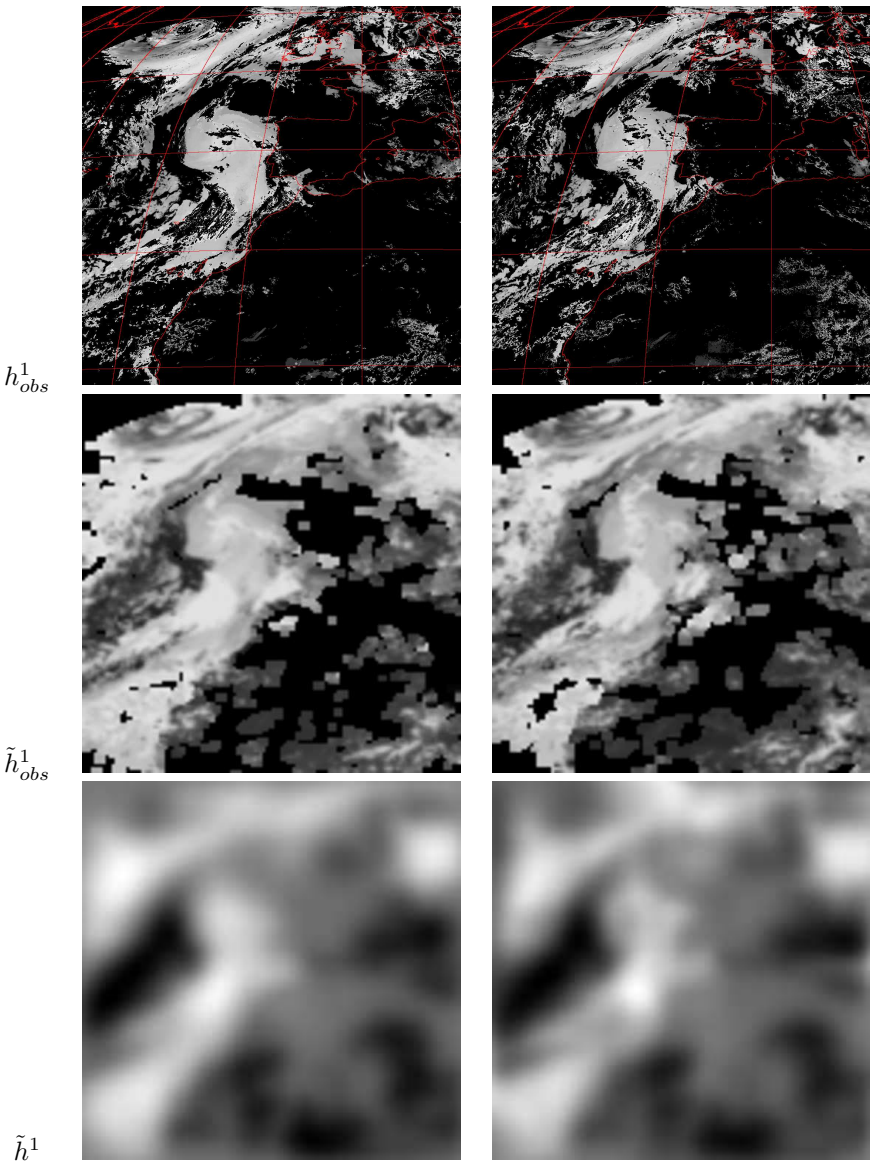

Figure 11: **Pressure difference reconstruction by assimilation with a perfect model.** Pressure difference observations h^k_{obs}, filtered observations $\tilde{h}^k_{obs}$ and reconstructed maps $\tilde{h}^k$ for the lower layer. Black regions of h^k_{obs} correspond to missing pressure difference observations and red lines represent coastal contours, meridians and parallels (every 10^o).

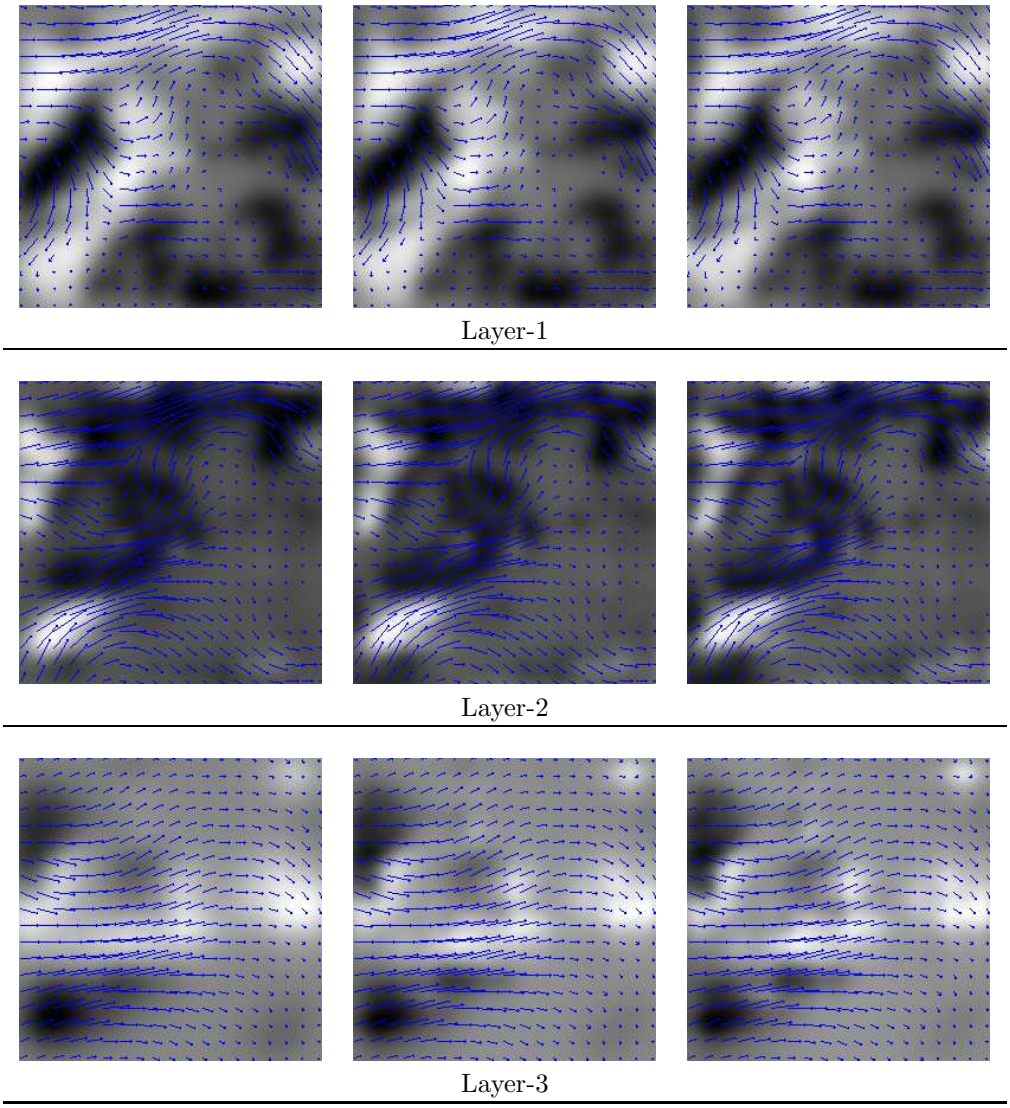

Figure 12: **Horizontal wind fields estimated by assimilation with a perfect model.** Estimates obtained by assimilation are superimposed on reconstructed pressure maps.

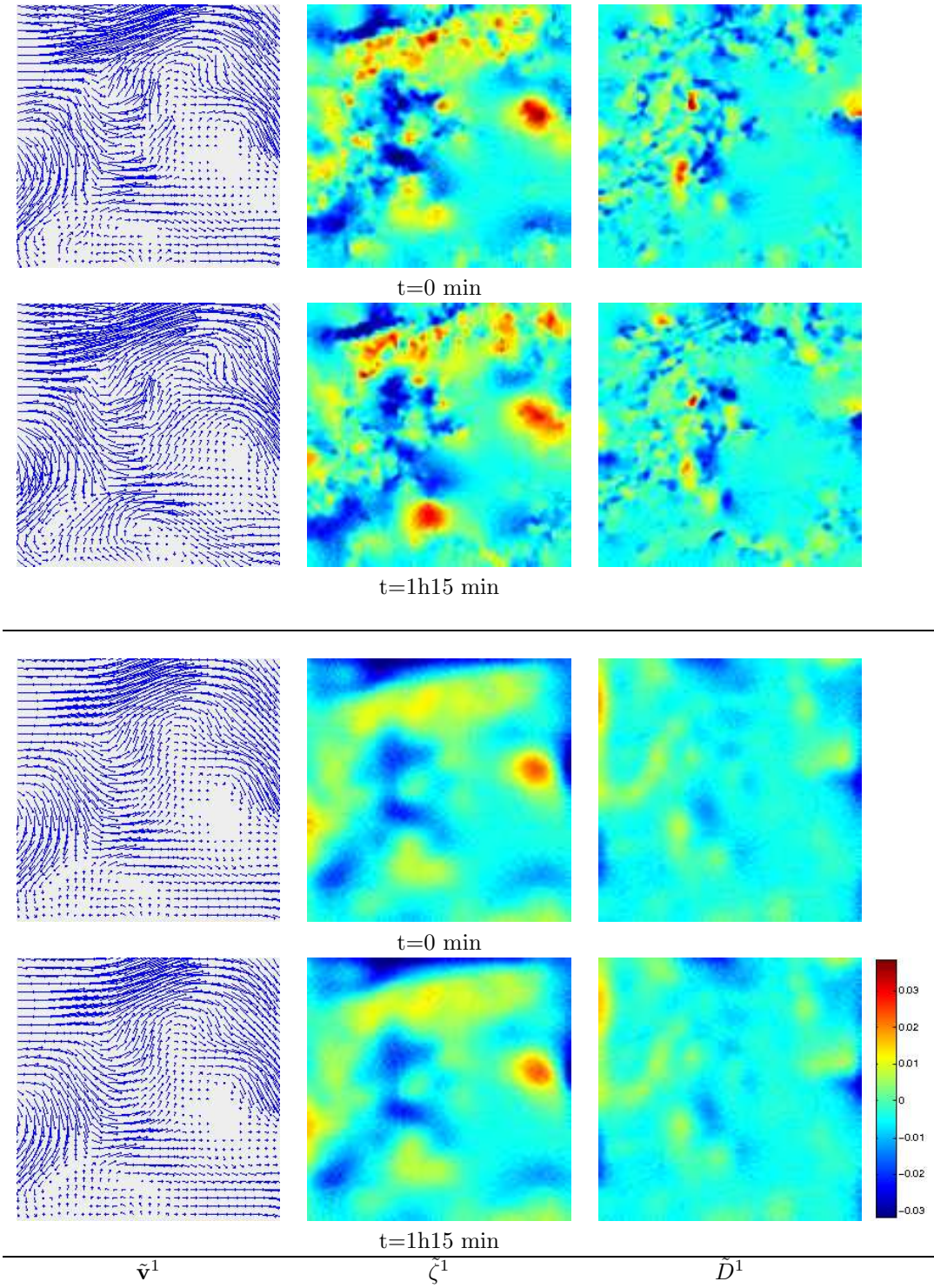

Figure 13: **Comparison of a reference optic-flow method (two first lines) with assimilation with perfect modeling (two last lines) .** Divergence $\tilde{D}^1$, vorticity $\tilde{\zeta}^1$ and wind $\tilde{\mathbf{v}}^1$ of the lower layer estimated by a reference optic-flow method and by assimilation with a perfect model.

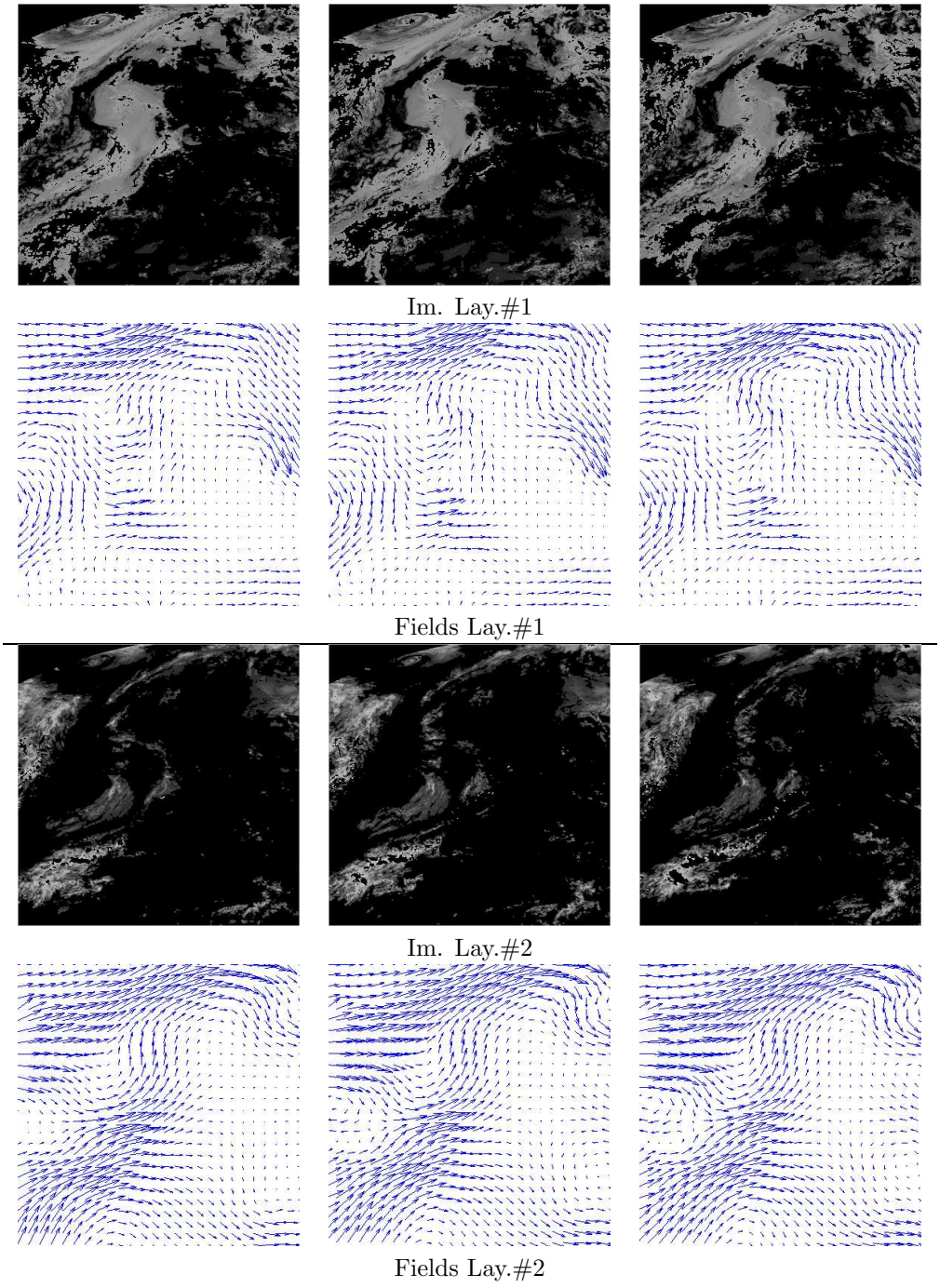

Figure 14: **Horizontal wind fields estimated by assimilation with an imperfect modeling (layers #1 and #2).** Filtered observations (top) and estimates (bottom) obtained by assimilation.

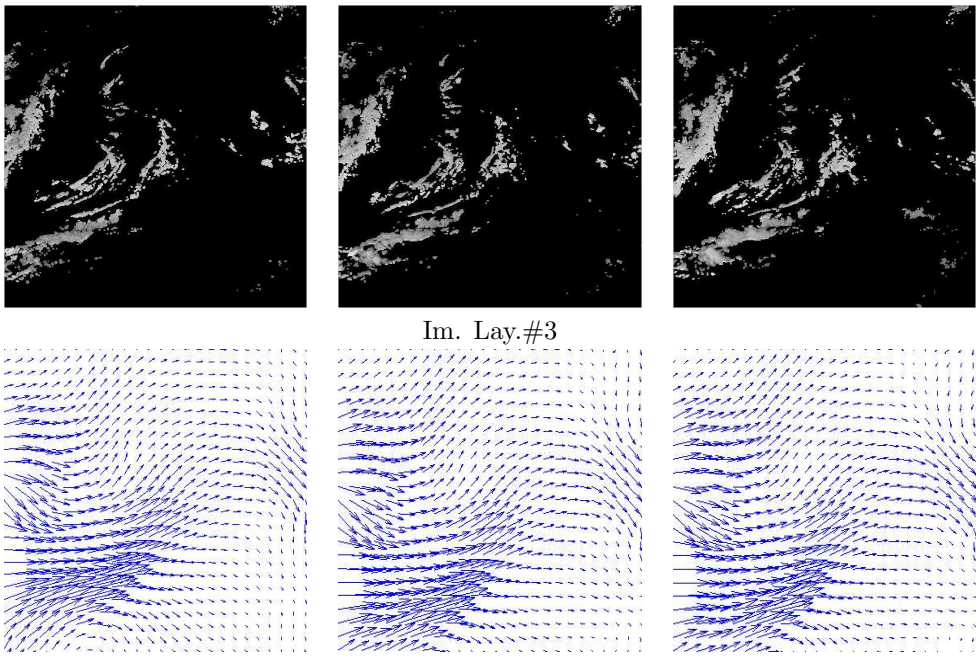

Figure 15: **Horizontal wind fields estimated by assimilation with an imperfect modeling (layer #3).** Filtered observations (top) and estimates (bottom) obtained by assimilation.

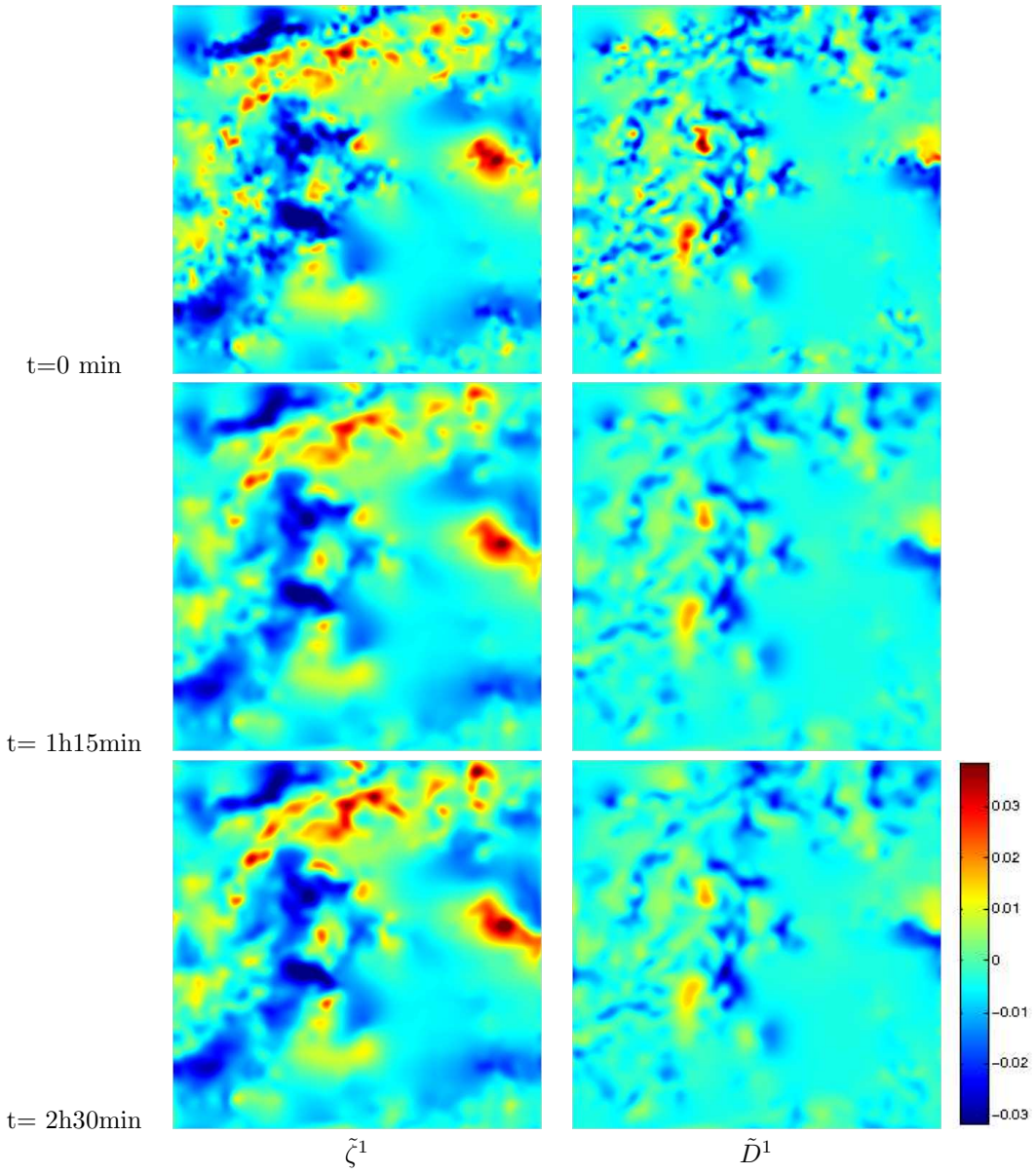

Figure 16: **Vorticity and divergence estimated by assimilation with imperfect modeling.** Divergence $\tilde{D}^1$ and vorticity $\tilde{\zeta}^1$ of the lower layer at different times.

However, on the contrary to the latter method which produces noisy and discontinuous fields, the proposed estimation method produces dynamically consistent estimates.

The assimilation scheme using an imperfect model proved also to be much more stable than the perfect modeling approach. Thus, in this case, observations $\tilde{h}^k_{obs}$ were filtered according to a normal parameter value $\delta_x = 100\delta_p^{-1}$.

7 Conclusions

In this paper, we proposed two assimilation approaches enabling, for the first, time dynamically consistent estimations of dense and layered atmospheric wind fields from entire satellite image sequences.

Both motion estimators are applied to sparse pressure difference images corresponding to a stack of layers in a stratified atmosphere. A method is proposed to derive such images from top of cloud pressure images and classification, which are operational satellite products of the EUMETSAT consortium.

The first estimator is based on an exact shallow water model describing the coupled evolution of the layer motion and thickness. A perfect modeling approach has been chosen in this first case in order to jointly assimilate pressure difference and wind variables through the control of the initial state. This first approach results therefore in reconstructed pressure difference maps and dense wind field estimates.

The second estimator is based on an imperfect modeling scheme, which manages the error of an *a priori* dynamical model. This model is a simplification of the previous shallow water dynamics in which the momentum equation has been made independent of layer thickness. This second approach therefore assimilates motion based on a vorticity-divergence evolution model without reconstructing pressure difference maps. Instead of using the shallow-water mass conservation model to control the evolution of pressure difference variables, this strategy uses mass conservation in order to build an image-adapted observation operator which is able to extract motion at fine spatio-temporal scales.

An evaluation first performed on synthetic image sequences demonstrated the efficiency of both methods in estimating accurately dense wind fields in the difficult case of noisy and sparse observations. Experiments performed on METEOSAT top of cloud pressure image sequences proved that both estimators were able to characterize time-consistent wind fields at large scales. Dynamical structures at finer-scale were better characterized using the imperfect assimilation scheme.

References

[1] A. Bennet. *Inverse Methods in Physical Oceanography*. Cambridge University Press, 1992.

[2] F. Bouttier and P. Courtier. Data assimilation concepts and methods. *ECMWF Meteorological Training Course Lecture Series*, 1999.

[3] T. Corpetti, D. Heitz, G. Arroyo, E. Mémin, and A. Santa-Cruz. Fluid experimental flow estimation based on an optical-flow scheme. *Experiments in fluids*, 40:80–97, 2006.

[4] T. Corpetti, E. Mémin, and P. Pérez. Dense estimation of fluid flows. *IEEE Trans. Pattern Anal. Machine Intell.*, 24(3):365–380, 2002.

[5] P. Courtier and O. Talagrand. Variational assimilation of meteorological observations with the direct and adjoint shallow-water equations. *Tellus*, 42:531–549, 1990.

[6] A. Cuzol, P. Hellier, and E. Memin. A low dimensional fluid motion estimator. *Accepted for publication in Int. J. of Comput. Vis.*, 2007.

[7] J. D'Adamo, N. Papadakis, E. Mémin, and A. G. Variational assimilation of pod low-order dynamical systems. *Journal of Turbulence*, 8(9):1–22, 2007.

[8] P. De Mey. Data assimilation at th oceanic mesoscale: a review. *J. Meteor. Soc. Jap.*, 75:415–427, 1997.

[9] A. de Saint-Venant. Théorie du mouvement non-permanent des eaux, avec application aux crues des rivières et à l'introduction des marées dans leur lit. *C. R. Acad. Sc. Paris*, 73:147–154, 1871.

[10] U. Frisch. *Turbulence : the legacy of A.N. Kolmogorov*. Cambridge university press, 19.

[11] D. Geman and G. Reynolds. Constrained restoration and the recovery of discontinuities. *IEEE Trans. Pattern Anal. Machine Intell.*, 14(3):367–383, 1992.

[12] Ghil and P. Malanotte-Rizzoli. Data assimilation in meteorology and oceanography. *Adv. Geophys.*, 23:141–266, 1991.

[13] P. Heas and Mémin. 3d motion estimation of atmospheric layers from image sequences. *IEEE Trans. Geoscience and Remote Sensing*, to appear 2007.

[14] P. Héas, E. Mémin, N. Papadakis, and A. Szantai. Layered estimation of atmospheric mesoscale dynamics from satellite imagery. *IEEE Trans. Geoscience and Remote Sensing*, 2007.

[15] P. Holland and R. Welsch. Robust regression using iteratively reweighted least-squares. *Commun. Statis.-Theor. Meth.*, A6(9):813–827, 1977.

[16] J. Holton. *An introduction to dynamic meteorology*. Academic press, 1992.

[17] M. Honnorat, F.-X. Le Dimet, and J. Monnier. On a river hydraulics model and Lagrangian data assimilation. In *International Conference on Adaptive Modeling and Simulation, ADMOS'05*, Barcelona, 2005.

[18] B. Horn and B. Schunck. Determining optical flow. *Artificial Intelligence*, 17:185–203, 1981.

[19] A. Kurganov and E. Tadmor. New high-resolution central schemes for nonlinear conservation laws and convetion-diffusion equations. *J. Comput. Phys.*, 160(1):241–282, 2000.

[20] F.-X. Le Dimet and J. Blum. Assimilation de données pour les fluides géophysiques. *MATAPLI, Bulletin de la SMAI*, 67:35–55, January 2002.

[21] F.-X. Le Dimet and O. Talagrand. Variational algorithms for analysis and assimilation of meteorological observations: theoretical aspects. *Tellus*, pages 97–110, 1986.

[22] J. Leese, C. Novack, and B. Clark. An automated technique for obtained cloud motion from geosynchronous satellite data using cross correlation. *Journal of applied meteorology*, 10:118–132, 1971.

[23] J. Lions. *Optimal control of systems governed by PDEs*. Springer-Verlag, 1971.

[24] B. Lucas and T. Kanade. An iterative image registration technique with an application to stereovision. In *Int. Joint Conf. on Artificial Intel. (IJCAI)*, pages 674–679, 1981.

[25] N. N. Mansour, J. H. Ferziger, and W. C. Reynolds. Large-eddy simulation of a turbulent mixing layer. Technical report, Report TF-11, Thermosciences Div., Dept. of Mech. Eng., Standford University, 1978.

[26] E. Mémin and P. Pérez. Dense estimation and object-based segmentation of the optical flow with robust techniques. *IEEE Trans. Image Processing*, 7(5):703–719, 1998.

[27] B. Oksendal. *Stochastic differential equations*. Spinger-Verlag, 1998.

[28] N. Papadakis, T. Corpetti, and E. Mémin. Dynamically consistent optical flow estimation. In *IEEE Int. Conf. Comp. Vis.(ICCV'07)*, October 2007.

[29] N. Papadakis and Mémin. A variational method for joint tracking of curve and motion. Technical Report 6283, INRIA Resarch report, September 2007.

[30] N. Papadakis and E. Mémin. Variational optimal control technique for the tracking of deformable objects. In *IEEE Int. Conf. Comp. Vis.(ICCV'07)*, October 2007.

[31] P. Ruhnau and C. Schnörr. Optical stokes flow estimation: An imaging-based control approach. *Exp.in Fluids*, 42(1):61–78, 2007.

[32] P. Sagaut. *Large-eddy simulation for incompressible flow - An introduction, third edition*. Springer-Verlag, Scientic Computation series, 2005.

[33] J. Schmetz, K. Holmlund, J. Hoffman, B. Strauss, B. Mason, V. Gaertner, A. Koch, and L. V. D. Berg. Operational cloud-motion winds from meteosat infrared images. *Journal of Applied Meteorology*, 32(7):1206–1225, 1993.

[34] J. Smagorinsky. General circulation experiments with the primitive equations. *Monthly Weather Review*, 91(3):99–164, 1963.

[35] O. Talagrand. Assimilation of observations, an introduction. *J. Meteor. Soc. Jap.*, 75:191–209, 1997.

[36] O. Talagrand and P. Courtier. Variational assimilation of meteorological observations with the adjoint vorticity equation. I: Theory. *J. of Roy. Meteo. soc.*, 113:1311–1328, 1987.

[37] G. Taylor. The transport of vorticity and heat through fluids in turbulent motion. In *Proc London Math Soc. Ser A*, pages 151–421, 1932.

[38] J. Templeton, M. Wang, and P. Moin. An efficient wall model for large-eddy simulation based on optimal control theory. *Phys. of Fluids*, 18(2), 2006.

[39] Z. Xu and C.-W. Shu. Anti-diffusive finite difference weno methods for shallow water with transport of pollutant. *Journal of Computational Mathematics*, 24:239–251, 2006.

[40] I. Yu. Gejadze, G. Copeland, and I. Navon. Open boundary control problem for navier-stokes equations including a free surface: Data assimilation. *Comput. Math. Appl.*, 52(8-9):1269–1288, 2006.

[41] J. Yuan, C. Schnoerr, and E. Mémin. Discrete orthogonal decomposition and variational fluid flow estimation. *J. of Math. Imaging and Vision*, 28(1):67–80, 2007.

[42] L. Zhou, C. Kambhamettu, and D. Goldgof. Fluid structure and motion analysis from multi-spectrum 2D cloud images sequences. In *Proc. Conf. Comp. Vision Pattern Rec.*, volume 2, pages 744–751, Hilton Head Island, USA, 2000.

Contents

Centre de recherche INRIA Rennes – Bretagne Atlantique
IRISA, Campus universitaire de Beaulieu - 35042 Rennes Cedex (France)

Centre de recherche INRIA Bordeaux – Sud Ouest : Domaine Universitaire - 351, cours de la Libération - 33405 Talence Cedex
Centre de recherche INRIA Grenoble – Rhône-Alpes : 655, avenue de l'Europe - 38334 Montbonnot Saint-Ismier
Centre de recherche INRIA Lille – Nord Europe : Parc Scientifique de la Haute Borne - 40, avenue Halley - 59650 Villeneuve d'Ascq
Centre de recherche INRIA Nancy – Grand Est : LORIA, Technopôle de Nancy-Brabois - Campus scientifique
615, rue du Jardin Botanique - BP 101 - 54602 Villers-lès-Nancy Cedex
Centre de recherche INRIA Paris – Rocquencourt : Domaine de Voluceau - Rocquencourt - BP 105 - 78153 Le Chesnay Cedex
Centre de recherche INRIA Saclay – Île-de-France : Parc Orsay Université - ZAC des Vignes : 4, rue Jacques Monod - 91893 Orsay Cedex
Centre de recherche INRIA Sophia Antipolis – Méditerranée : 2004, route des Lucioles - BP 93 - 06902 Sophia Antipolis Cedex

Éditeur
INRIA - Domaine de Voluceau - Rocquencourt, BP 105 - 78153 Le Chesnay Cedex (France)
http://www.inria.fr
ISSN 0249-6399